LJMU Research Online

Cautun, M, Benitez-Llambay, A, Deason, AJ, Frenk, CS, Fattahi, A, Gomez, FA, Grand, RJJ, Oman, KA, Navarro, JF and Simpson, CM

 The milky way total mass profile as inferred from Gaia DR2

http://researchonline.ljmu.ac.uk/id/eprint/19308/

Article

For more information please contact researchonline@ljmu.ac.uk

The milky way total mass profile as inferred from *Gaia* DR2

Marius Cautun [1,2]★ Alejandro Benítez-Llambay,[2] Alis J. Deason [2] Carlos S. Frenk,[2]
Azadeh Fattahi [2] Facundo A. Gómez,[3,4] Robert J. J. Grand [5] Kyle A. Oman [2]
Julio F. Navarro[6] and Christine M. Simpson [7,8]

[1]*Leiden Observatory, Leiden University, PO Box 9513, NL-2300 RA Leiden, the Netherlands*
[2]*Institute of Computational Cosmology, Department of Physics, Durham University, South Road, Durham DH1 3LE, UK*
[3]*Instituto de Investigación Multidisciplinar en Ciencia yTecnología, Universidad de La Serena, Raúl Bitrán 1305, La Serena, Chile*
[4]*Departamento de Física y Astronomía, Universidad de LaSerena, Av. Juan Cisternas 1200 N, La Serena, Chile*
[5]*Max-Planck-Institut für Astrophysik, Karl-Schwarzschild-Str. 1, D-85748 Garching, Germany*
[6]*Department of Physics and Astronomy, University of Victoria, Victoria, BC V8P 5C2, Canada*
[7]*Enrico Fermi Institute, The University of Chicago, Chicago, IL 60637, USA*
[8]*Department of Astronomy and Astrophysics, The University of Chicago, Chicago, IL 60637, USA*

ABSTRACT

We determine the Milky Way (MW) mass profile inferred from fitting physically motivated models to the *Gaia* DR2 Galactic rotation curve and other data. Using various hydrodynamical simulations of MW-mass haloes, we show that the presence of baryons induces a contraction of the dark matter (DM) distribution in the inner regions, $r \lesssim 20$ kpc. We provide an analytic expression that relates the baryonic distribution to the change in the DM halo profile. For our galaxy, the contraction increases the enclosed DM halo mass by factors of roughly 1.3, 2, and 4 at radial distances of 20, 8, and 1 kpc, respectively compared to an uncontracted halo. Ignoring this contraction results in systematic biases in the inferred halo mass and concentration. We provide a best-fitting contracted NFW halo model to the MW rotation curve that matches the data very well.[1] The best-fit has a DM halo mass, $M_{200}^{\mathrm{DM}} = 0.97_{-0.19}^{+0.24} \times 10^{12}\,\mathrm{M}_\odot$, and concentration before baryon contraction of $9.4_{-2.6}^{+1.9}$, which lie close to the median halo mass–concentration relation predicted in ΛCDM. The inferred total mass, $M_{200}^{\mathrm{total}} = 1.08_{-0.14}^{+0.20} \times 10^{12}\,\mathrm{M}_\odot$, is in good agreement with recent measurements. The model gives an MW stellar mass of $5.04_{-0.52}^{+0.43} \times 10^{10}\,\mathrm{M}_\odot$ and infers that the DM density at the Solar position is $\rho_\odot^{\mathrm{DM}} = 8.8_{-0.5}^{+0.5} \times 10^{-3}\,\mathrm{M}_\odot\,\mathrm{pc}^{-3} \equiv 0.33_{-0.02}^{+0.02}\,\mathrm{GeV\,cm}^{-3}$. The rotation curve data can also be fitted with an uncontracted NFW halo model, but with very different DM and stellar parameters. The observations prefer the physically motivated contracted NFW halo, but the measurement uncertainties are too large to rule out the uncontracted NFW halo.

Key words: Galaxy: fundamental parameters – Galaxy: halo – Galaxy: kinematics and dynamics – Galaxy: structure – galaxies: haloes.

1 INTRODUCTION

The wealth of data available for the Milky Way (MW) makes our galaxy an unmatched laboratory for testing cosmology on the smallest scales and for understanding galaxy formation physics in detail (e.g. see the reviews by Bullock & Boylan-Kolchin 2017; Zavala & Frenk 2019). The results of many of these tests are

sensitive to the dark matter (DM) content of our galaxy and, in particular, to the total mass and the radial density profile of our Galactic halo. For example, the total number of subhaloes is very sensitive to the host halo mass (e.g. Purcell & Zentner 2012; Wang et al. 2012; Cautun et al. 2014a; Hellwing et al. 2016) while the radial mass profile plays a key role in determining the orbits of satellite galaxies and tidal streams (e.g. Barber et al. 2014; Fritz et al. 2018; Cautun et al. 2019; Garavito-Camargo et al. 2019; Monachesi et al. 2019a). The number and orbits of satellites are a key test of properties of the DM, such as the mass of the DM particle and its interaction cross-section (e.g. Peñarrubia et al. 2010;

★ E-mail: marius.cautun@gmail.com
[1]The data products are publicly available in Cautun & Callingham (2020) at: https://github.com/MariusCautun/Milky_Way_mass_profile

Vogelsberger, Zavala & Loeb 2012; Kennedy et al. 2014; Lovell et al. 2014; Cautun & Frenk 2017; Kahlhoefer et al. 2019), and also constrain galaxy formation models (e.g. Sawala et al. 2016a, b; Bose, Deason & Frenk 2018; Shao et al. 2018a; Fillingham et al. 2019).

Most previous studies have focused on determining the total mass of the Galactic DM halo using a variety of methods, such as the dynamics of the stellar halo (e.g. Xue et al. 2008; Deason et al. 2012; Kafle et al. 2012), globular clusters (e.g. Eadie & Harris 2016; Posti & Helmi 2019; Watkins et al. 2019), and satellite galaxies (e.g. Watkins, Evans & An 2010; Li et al. 2017; Patel, Besla & Mandel 2017; Callingham et al. 2019), high velocity stars (e,g, Smith et al. 2007; Piffl et al. 2014; Fragione & Loeb 2017; Rossi et al. 2017; Deason et al. 2019a), the orbits of tidal streams (e.g. Gibbons, Belokurov & Evans 2014; Bowden, Belokurov & Evans 2015), the luminosity function of the MW satellites (e.g. Busha et al. 2011; Cautun et al. 2014b), and the dynamics of the Local Group (e.g. Li & White 2008; Diaz et al. 2014; Peñarrubia et al. 2016). However, recent estimates of the total mass of the MW still range within about a factor of two (see e.g. fig. 7 in Callingham et al. 2019), reflecting systematics in many of the methods used to infer it (e.g Wang et al. 2015, 2017, 2018).

The radial density profile of the MW is even more poorly measured due to a lack of data outside ∼20 kpc and uncertainties in modelling the effect of baryons on the DM halo. Most studies assume that the DM halo is well described by an NFW profile (Navarro, Frenk & White 1996, 1997) and constrain the profile by two parameters, such as total mass and concentration (e.g. McMillan 2011; Bovy et al. 2012; Eilers et al. 2019). Such studies argue that the Galactic halo has a very high concentration, typically ∼14 or higher (e.g. Deason et al. 2012; Kafle et al. 2014; McMillan 2017; Monari et al. 2018; Lin & Li 2019), that is in tension with theoretical expectations based on cosmological simulations, which predict a mean concentration of ∼9 and a 68 percentile range of ∼[7, 12] (Ludlow et al. 2014; Hellwing et al. 2016; Klypin et al. 2016).

The higher than expected concentration of the MW halo could be a manifestation of the contraction of the DM halo induced by the presence of a galaxy at its centre (e.g. Schaller et al. 2015; Dutton et al. 2016; Lovell et al. 2018). For MW and higher mass haloes, the effect of baryons on the DM halo is well described by the adiabatic contraction model (Callingham et al. 2020), in which baryons slowly accumulate at the halo centre and the DM distribution distorts in such a way that its action integrals remain approximately constant (Barnes & White 1984; Blumenthal et al. 1986; Barnes 1987). This process can be implemented analytically if the distribution of DM actions in the absence of baryons is known (Sellwood & McGaugh 2005); however, since this is not well known and there is halo-to-halo variation, in practice most studies have used approximations of this process (e.g. see Blumenthal et al. 1986; Abadi et al. 2010; Gnedin et al. 2010). Such approaches have only occasionally been used when analysing MW data (e.g. Piffl, Penoyre & Binney 2015; Cole & Binney 2017), and most studies ignore the change in the DM profile induced by the condensation of baryons at the centre of haloes, despite, as we shall see, the fact that it is a large effect, especially in the inner 10 kpc of our galaxy.

In this paper, we provide a best-fitting mass model for the MW using the latest *Gaia* rotation curve (Eilers et al. 2019) combined with the robust and extensively tested total mass determination of Callingham et al. (2019). We improve on previous studies by modelling the contraction of the DM halo induced by the central galaxy. We study the DM halo contraction and propose a simple parametric model based on the predictions of three state-of-the-art galaxy formation simulations: Auriga (Grand et al. 2017), APOSTLE (Fattahi et al. 2016; Sawala et al. 2016b) and EAGLE (Schaye et al. 2015), and find that all three simulations predict the same DM halo contraction within the limits of halo-to-halo variation. We show that the contracted DM halo cannot be modelled as a pure NFW profile and even more flexible formulae, such as the generalized NFW profile (gNFW, which has been used to model the MW halo – McMillan 2017; Karukes et al. 2019b), struggle to describe the radial profile of the contracted halo.

We model the MW galaxy using seven components (similar to the approach used by McMillan 2017): a bulge, a thin and a thick stellar disc, an HI and a molecular gas disc, a circumgalactic medium (CGM) component, and a DM halo. Our main results are for a DM halo that has been contracted according to the self-consistently determined MW stellar mass. For comparison, we use a second model in which the DM halo is taken as an NFW profile. While both models fit the data equally well, the former (i.e. the contracted halo) is more physically motivated and is also the one whose predictions agree best with other independent observations. In particular, our contracted halo has the typical concentration of a ∼10^{12} M$_\odot$ halo as predicted by numerical simulations (without imposing any prior on the concentration), corresponds to a more massive halo than in the pure NFW case, and also favours an MW stellar mass ∼20 per cent lower than the NFW case. We show that the two cases can be distinguished using three diagnostics: (i) the stellar mass of the MW, (ii) the rotation curve between 1 and 5 kpc, and (iii) an accurate determination of the total halo mass.

This paper is structured as follows. In Section 2 we describe our model for the various MW baryonic components. In Section 3 we characterize how the DM distribution changes in response to the accumulation of baryons at the halo centre, which we study using hydrodynamical simulations. Section 4 describes how much we expect the Galactic DM halo to contract given the distribution of visible matter in the MW. Section 5 presents our best fit model to the MW rotation curve. The results are discussed and interpreted in Section 6. We conclude with a short summary in Section 7.

2 THE MW BARYONIC COMPONENTS

The goal of this paper is to infer the mass profile of the MW, and in particular the profile of the DM halo. To do so, we first need to specify the baryon distribution in the MW, which we model using a bulge, a thin, and a thick stellar disc; an HI disc and a molecular gas disc; and a diffuse gaseous halo. The first five of this baryonic components are the same that McMillan (2017) considered, but some of the parameter values we adopt are different since they correspond to the best fitting values to the data, as we will describe in Section 5. The mass and profile of the Galactic gaseous halo (i.e. the circumgalactic medium, hereafter CGM) is unconstrained; however, both analytical arguments (White & Frenk 1991) and hydrodynamical simulations (e.g Schaye et al. 2015), suggest that it contains the majority of the baryonic mass at large distances from the Galactic Centre. Section 2.4 presents our best model for the MW CGM. The MW also has a stellar halo, but its mass is insignificant, roughly 3 per cent of the total Galactic stellar mass (Deason, Belokurov & Sanders 2019b), and thus we neglect this Galactic component.

Table 1. The parameters of the MW components that are kept fixed when fitting our model to observations.

Component	Expression	Parameters
Bulge	equation (1)	$r_0 = 75$ pc, $r_{cut} = 2.1$ kpc, $\alpha = 1.8$, $q = 0.5$
Thin disc	equation (3)	$z_{d, thin} = 300$ pc
Thick disc	equation (3)	$z_{d, thick} = 900$ pc
H I disc	equation (4)	$z_d = 85$ pc, $R_m = 4$ kpc, $R_d = 7$ kpc, $\Sigma_0 = 53$ M$_\odot$ pc^{-2}
H$_2$ disc	equation (4)	$z_d = 45$ pc, $R_m = 12$ kpc, $R_d = 1.5$ kpc, $\Sigma_0 = 2200$ M$_\odot$ pc^{-2}
CGM	equation (5)	$A_{CGM} = 0.190$, $\beta_{CGM} = -1.46$

2.1 Bulge

We model the MW bulge using the McMillan (2017) profile (which is an axisymmetric form of the model proposed by Bissantz & Gerhard 2002) given by,

$$\rho_{bulge} = \frac{\rho_{0,bulge}}{(1 + r'/r_0)^\alpha} \exp\left[- \left(r'/r_{cut} \right)^2 \right], \qquad (1)$$

where, r' represents a combination of the cylindrical coordinates (R, z) (where R is in the plane of the MW disc and z perpendicular to this plane):

$$r' = \sqrt{R^2 + (z/q)^2}. \qquad (2)$$

The remaining quantities, α, r_0, r_{cut}, and the axial ratio, q, are model parameters whose values are listed in Table 1 and kept fixed for the remainder of this analysis. The parameter, $\rho_{0,bulge}$, denotes the central stellar density which is allowed to vary according to the Gaussian prior given in Table 2. We note that there is still a large degree of uncertainty regarding the exact mass and profile of the MW bulge (e.g. see the compilations of Iocco, Pato & Bertone 2015; Bland-Hawthorn & Gerhard 2016) and that our data, which cover only distances beyond 5 kpc from the Galactic Centre, are not able to provide any meaningful constraints on the bulge mass or its radial profile. Also, for the same reason we do not model the complicated geometry of the stellar distribution at the centre of the MW, i.e. peanut bulge and bar (e.g. Portail et al. 2017), since it has only minor effects on the gravitational field at $R > 5$ kpc.

2.2 Thin and thick stellar discs

We model the MW stellar distribution as consisting of two components, a thin and a thick disc (e.g. Jurić et al. 2008; Pouliasis, Di Matteo & Haywood 2017), with each component described by the exponential profile:

$$\rho_d(R, z) = \frac{\Sigma_0}{2z_d} \exp\left(- \frac{|z|}{z_d} - \frac{R}{R_d} \right), \qquad (3)$$

where z_d denotes the disc scale-height, R_d is the disc scale-length, and Σ_0 is the central surface density. For the scale-height, we take the values derived by Jurić et al. (2008), who find that $z_d = 300$ and 900 pc for the thin and thick discs respectively (see also the recent analyses of the *Gaia* and DES data: Mateu & Vivas 2018; Pieres et al. 2019). We note that the exact value of z_d does not significantly affect the inferred MW mass model – see e.g. McMillan (2011). The other two parameters of each disc model, R_d and Σ_0, are derived from the data as we will discuss in Section 5. When deriving the scale-length for both the thin and thick discs, we used the Gaussian prior given in the fourth column of Table 2, which

is based on the typical scatter in R_d amongst different studies (see the compilation of measurements in Bland-Hawthorn & Gerhard 2016).

2.3 H I and molecular discs

The next two components of the MW are the H I and the molecular gas distributions, which can account for a significant fraction of the baryonic mass and, since they have a different geometry from the stellar component, cannot be easily treated as part of the stellar disc (Kalberla & Dedes 2008). Instead, we model these two components as an exponentially declining disc-like geometry given by (Kalberla & Dedes 2008)

$$\rho_d(R, z) = \frac{\Sigma_0}{4z_d} \exp\left(- \frac{R_m}{R} - \frac{R}{R_d} \right) \mathrm{sech}^2\left(\frac{z}{2z_d} \right), \qquad (4)$$

where, as in the stellar disc case, Σ_0 denotes the central surface density, z_d the scale-height, and R_d the scale-length of the disc. This disc has a inner hole whose size is controlled by the scale-length, R_m. In general, the mass and geometry of the MW gas distribution are still uncertain (e.g. see discussions in Kalberla & Dedes 2008; Heyer & Dame 2015); however, they are reasonably well known at the Sun's position. We take the H I and molecular gas parameters from McMillan (2017) determined by matching the two gas discs to observational constraints around the Sun's position. For completeness, we give the values of these parameters in Table 1. They correspond to an H I mass of 1.1×10^{10} M$_\odot$ and a molecular gas mass of 10 per cent of the H I mass.

2.4 Circumgalactic medium

Galaxies are surrounded by an extended gaseous corona, the CGM, which consists mostly of hot, diffuse gas but also contains denser, colder clouds, some moving at high velocity. Due to its diffuse nature, the CGM is difficult to characterize in detail, and even more so in the case of our own galaxy where much of the X-ray emission from the hot gas is absorbed by neutral hydrogen in the disc (for details see the review by Tumlinson, Peeples & Werk 2017). However, the CGM can contain a large fraction of the baryonic mass within the diffuse halo and thus needs to be included when modelling the mass profile of the MW. Note that the CGM mostly contributes to the baryonic mass profile at large distances, $r \gtrsim 100$ kpc, from the Galactic Centre, while in the inner part most of the baryons are found in the disc. For our study, including the CGM does not significantly alter the inferred DM halo mass or concentration since these are mostly determined by the stellar circular velocity curve – see discussion in Section 5. However, the CGM does affect, at the $\sim$5 per cent level, the total mass within the radius, R_{200}, as well as the escape velocity at the Sun's position, which is determined by the total mass profile out to a distance of $2R_{200}$ (see Deason et al. 2019a).

Observationally, the total mass and density profile of the CGM in MW-mass galaxies are poorly determined and this is likely to remain so for years to come (e.g. Tumlinson et al. 2017). However, we can use hydrodynamical simulations to place constraints on the Galactic CGM. For this, we have measured in the three simulations described in Section 3.1, Auriga, APOSTLE and EAGLE_recal, the baryonic profile at distances, $r > 0.15R_{200}$, which, for the MW, would correspond to $r \gtrsim 30$ kpc. We find significant halo-to-halo scatter, which is indicative of the diversity of CGM distributions around MW-mass galaxies (Hani et al. 2019; Davies et al. 2020), but the median distribution shows

Table 2. The parameters of the MW components that are varied when fitting our model to observations. The columns are as follows: parameter description (1) and symbol denoting it (2); units (3); mean and standard deviation of the Gaussian prior (4); the MLE and the 68 percentile confidence interval for the model with a contracted NFW DM halo (5); and the MLE and the 68 percentile confidence interval for the model with an uncontracted NFW profile for the DM halo (6). For convenience and ease of use, the last rows of the table give derived quantities, such as bulge, disc, and total masses.

Quantity	Symbol	Units	Prior	Best fitting values	
				Contracted halo	NFW halo
Bulge density	$\rho_{0,\text{bulge}}$	$M_\odot\ \text{pc}^{-3}$	100 ± 10	103^{+10}_{-11}	101^{+12}_{-9}
Thin disc density	$\Sigma_{0,\text{thin}}$	$M_\odot\ \text{pc}^{-2}$	–	731^{+91}_{-112}	1070^{+47}_{-190}
Thick disc density	$\Sigma_{0,\text{thick}}$	$M_\odot\ \text{pc}^{-2}$	–	101^{+41}_{-65}	113^{+50}_{-60}
Thin disc scale length	R_{thin}	kpc	2.5 ± 0.5	$2.63^{+0.14}_{-0.12}$	$2.43^{+0.15}_{-0.07}$
Thick disc scale length	R_{thick}	kpc	3.5 ± 0.7	$3.80^{+0.54}_{-.89}$	$3.88^{+0.33}_{-0.96}$
DM mass within R_{200}	$M^{\text{DM}}_{200,\text{MW}}$	$10^{12}\ M_\odot$	–	$0.97^{+0.24}_{-0.19}$	$0.82^{+0.09}_{-0.18}$
Halo concentration[†]	$c^{\text{NFW}}_{\text{MW}}$		–	$9.4^{+1.9}_{-2.6}$	$13.3^{+3.6}_{-2.7}$
		Derived quantities			
Bulge mass	$M_{\star,\text{bulge}}$	$10^{10}\ M_\odot$	–	$0.94^{+0.09}_{-0.10}$	$0.92^{+0.11}_{-0.08}$
Thin disc mass	$M_{\star,\text{thin}}$	$10^{10}\ M_\odot$	–	$3.18^{+0.30}_{-0.45}$	$3.98^{+0.26}_{-0.67}$
Thick disc mass	$M_{\star,\text{thick}}$	$10^{10}\ M_\odot$	–	$0.92^{+0.19}_{-0.12}$	$1.07^{+0.18}_{-0.19}$
Total stellar mass	$M_{\star,\text{total}}$	$10^{10}\ M_\odot$	–	$5.04^{+0.43}_{-0.52}$	$5.97^{+0.40}_{-0.80}$
H I and molecular gas mass[‡]	$M_{\text{HI}+\text{H2}}$	$10^{10}\ M_\odot$	–	1.2	1.2
CGM mass within R_{200} [‖]	M_{CGM}	$10^{10}\ M_\odot$	–	6.4	5.5
Total mass within R_{200}	$M^{\text{total}}_{200,\text{MW}}$	$10^{12}\ M_\odot$	–	$1.08^{+0.20}_{-0.14}$	$0.95^{+0.10}_{-0.19}$
Halo scale radius	$R_{s;\ \text{MW}}$	kpc	–	$23.8^{+8.1}_{-6.2}$	$14.4^{+4.5}_{-3.5}$
Halo radius[★]	R_{200}	kpc	–	218^{+12}_{-18}	207^{+7}_{-15}

Notes. [†] The concentration is calculated with respect to R_{200} of the total (DM plus baryons) mass distribution. For the contracted halo model, the halo concentration corresponds to the value associated to the NFW profile that describes the halo before contraction.

[‡] The gas mass has been taken as constant and was not varied when fitting our model. We give it here for completeness.

[‖] The CGM mass is calculated as a fraction of 5.8 percent of the total mass within R_{200} – see discussion in Section 2.4.

[★] The halo radius, R_{200}, corresponds to the radius of a sphere whose mean enclosed total (DM plus baryons) density is 200 times the critical density.

good agreement between the three simulations. In particular, we find that the CGM mass within the halo radius, R_{200}, represents 5.8 ± 1.5 per cent of the total mass fraction, while within $2R_{200}$ the CGM mass fraction increases to 11.5 ± 2.5 per cent of the total mass (the errors correspond to the 68 per cent confidence interval and are due to halo-to-halo scatter). In terms of the cosmic mean baryon fraction, $f_{\text{bar}} = 15.7$ per cent for a Planck Collaboration XVI (2014) cosmology, the CGM corresponds to 37 and 73 per cent of the baryon budget expected within R_{200} and $2R_{200}$ respectively if the baryons followed the DM distribution.

We have assumed that the CGM radial density profile can be expressed as a power law of distance, i.e. $\rho_{\text{CGM}} \sim r^{\beta_{\text{CGM}}}$, and then, taking the CGM mass fractions within R_{200} and $2R_{200}$ to be 5.8 and 11.5 per cent respectively, we have estimated the power-law exponent as well as the overall density normalization. The resulting CGM density is given by:

$$\rho_{\text{CGM}} = 200\rho_{\text{crit}}\ A_{\text{CGM}}\ f_{\text{bar}} \left(\frac{r}{R_{200}}\right)^{\beta_{\text{CGM}}}, \qquad (5)$$

where ρ_{crit} is the critical density of the Universe, $A_{\text{CGM}} = 0.190$ is a normalization factor, and $\beta_{\text{CGM}} = -1.46$ is the index of the power

law. Then, the enclosed CGM mass within radius, r is, given by:

$$M_{\text{CGM}}(< r) = \frac{3A_{\text{CGM}}}{\beta_{\text{CGM}} + 3}\ f_{\text{bar}}\ M^{\text{tot}}_{200} \left(\frac{r}{R_{200}}\right)^{\beta_{\text{CGM}}+3}, \qquad (6)$$

where M^{tot}_{200} is the total mass within the halo radius R_{200}. For example, if the MW total mass is $1.0 \times 10^{12}\ M_\odot$, then the CGM mass within the halo radius is $5.9 \times 10^{10}\ M_\odot$, which is almost equal to the inner baryonic mass, that is the sum of the stellar components and the H I and H$_2$ gas discs.

3 DM HALO RESPONSE TO THE CENTRAL GALAXY

We now summarize the details of the three galaxy formation simulations, Auriga, APOSTLE, and EAGLE_recal, which we use to characterize the changes in the structure of DM haloes that result from the assembly of a galaxy at their centre. In Section 3.3 we compare each host halo in the hydrodynamics run with its counterpart in the DM-only (DMO) run. The goal is to find a parametric expression for the halo radial density profile given a distribution of baryons and then test how well it reproduces the contraction of individual DM haloes.

3.1 Simulations

The Auriga and EAGLE simulations assume the Planck Collaboration XVI (2014) cosmological parameters: $\Omega_m = 0.307$, $\Omega_b = 0.048$, $\Omega_\Lambda = 0.693$, and $H_0 = 100\,h\,\mathrm{km\,s^{-1}\,Mpc^{-1}}$, with $h = 0.6777$. The APOSTLE project assumes the *WMAP*7 cosmology (Komatsu et al. 2011), with parameters: $\Omega_m = 0.272$, $\Omega_b = 0.045$, $\Omega_\Lambda = 0.728$, and $h = 0.704$. In all the simulations, haloes are identified using the FOF algorithm (Davis et al. 1985) with a linking length 0.2 times the mean particle separation and further split into gravitationally bound substructures using the SUBFIND code (Springel, Yoshida & White 2001). We study only central galaxies, i.e. the most massive SUBFIND object associated with an FOF halo, whose centre is taken to be their most gravitationally bound particle. The haloes are characterized by the radius, R_{200}, of a sphere whose mean enclosed density is 200 times the critical density, and by the mass, M_{200}, contained within this radius.

3.1.1 Auriga

Auriga is a suite of high-resolution magnetohydrodynamical simulations of MW-mass haloes ran with the AREPO code (Springel 2010). The suite consist of 40 haloes, 30 of which have mass, $M_{200} \in [1, 2] \times 10^{12}\,\mathrm{M_\odot}$, and were first introduced in Grand et al. (2017), plus 10 additional lower mass haloes, with M_{200} masses just below $\sim 10^{12}\,\mathrm{M_\odot}$ (Grand et al. 2019a). The Auriga systems are zoom-in resimulations of MW-mass haloes selected from the EAGLE $100^3\,\mathrm{Mpc^3}$ periodic cube simulation (Schaye et al. 2015) that are relatively isolated at $z = 0$, that is have no objects more massive than half their halo mass within a distance of 1.37 Mpc. See Grand et al. 2017 for more details, as well as for illustrations and properties of the central galaxies in the Auriga haloes.

The Auriga simulations successfully reproduce many properties of observed central and satellite galaxies, such as the stellar masses and star formation rates of spirals (Grand et al. 2017; Marinacci et al. 2017), the density and kinematics of stellar haloes (Deason et al. 2017; Monachesi et al. 2019b), and the luminosity function of MW satellites (Simpson et al. 2018). Here, we use both resolution levels of the Auriga project: the medium resolution, or level 4, and the higher resolution, or level 3, simulation – only 6 systems were resimulated at this resolution. The level 4 runs have initial gas and DM particle masses of $5 \times 10^4\,\mathrm{M_\odot}$ and $3 \times 10^5\,\mathrm{M_\odot}$ respectively, and gravitational softening $\epsilon = 0.37$ kpc, while level 3 has a 8 times better mass resolution and 2 times better spatial resolution.

3.1.2 APOSTLE

APOSTLE is a suite of 12 pairs of MW-mass haloes selected to resemble the Local Group in terms of mass, separation, relative velocity, and local environment (Fattahi et al. 2016; Sawala et al. 2016a). They were selected from a DMO simulation of a $100^3\,\mathrm{Mpc^3}$ periodic cube, known as COLOR (Hellwing et al. 2016), and were resimulated at three resolution levels. Here we have used the medium resolution runs, which have an initial gas particle mass of $\sim 1.2 \times 10^5\,\mathrm{M_\odot}$ and gravitational softening $\epsilon = 0.31$ kpc, and the four volumes (8 haloes in total) simulated at 12 times higher mass resolution and $12^{1/3}$ better spatial resolution. Each APOSTLE volume contains two galactic-size haloes, corresponding to the MW and M31, and here we use both haloes of each pair.

The APOSTLE simulations were run with a modified version of the GADGET 3 code (Springel 2005) with the reference EAGLE

galaxy formation models (Crain et al. 2015; Schaye et al. 2015), which were calibrated to reproduce the galaxy mass function, galaxy sizes, and the relation between black hole mass and galaxy mass. The EAGLE model reproduces galaxy rotation curves (Schaller et al. 2015), the bimodal distribution of star formation rates and the cosmic star formation history (Furlong et al. 2015), the Hubble sequence of galaxy morphologies (Trayford et al. 2015) and the Tully-Fisher relation over a wide range of galaxy masses (Ferrero et al. 2017).

3.1.3 EAGLE_recal

We have also used the MW-mass haloes from the L025N0752 box of the EAGLE project run with the recal model (labelled as Recal-L025N0752). We refer to this run as EAGLE_recal hereafter. This consists of a cosmological volume simulation in a periodic cube of side-length 25 Mpc with a mass resolution 8 times better than the fiducial EAGLE simulation. The simulation contains 752^3 DM particles with mass of $1.2 \times 10^6\,\mathrm{M_\odot}$ and a similar number of baryonic particles with initial mass $2.3 \times 10^5\,\mathrm{M_\odot}$ respectively, and gravitational softening $\epsilon = 0.35$ kpc (for more details see Schaye et al. 2015). The EAGLE_recal simulation has been run using the same galaxy formation model as the standard EAGLE run, but with recalibrated parameter values that account for the higher mass resolution of the EAGLE_recal run. The EAGLE_recal galaxies match observed galaxy properties at least to the same extent (and in some cases better) than the standard EAGLE galaxies (e.g. see Furlong et al. 2015; Schaller et al. 2015; Schaye et al. 2015).

The APOSTLE and EAGLE_recal simulations have a similar implementation of galaxy formation processes, but use different parameter values, and thus we expect them to make similar predictions. There are clear advantages in studying the halo and galaxies in the two samples, since we can test the robustness of the results against changes in mass resolution as well as in some of the parameters describing the subgrid galaxy formation models. Furthermore, with EAGLE_recal we can study the effect of galaxy assembly in a much larger sample of objects than in APOSTLE and thus better characterize the halo-to-halo variation.

We select from the EAGLE_recal simulation Galactic mass haloes, that is haloes which, in the DMO version of the simulation, have mass, $M_{200} \in [0.7, 3] \times 10^{12}\,\mathrm{M_\odot}$, and whose counterpart in the hydrodynamic simulation is also a main halo. These selection criteria results in 34 haloes.

3.2 Sample selection

For all three simulation suites we make use of the hydrodynamics and DMO versions. Finding the counterpart of a DMO halo in the hydrodynamic simulation and viceversa is straightforward since we are only interested in main haloes, not subhaloes.

Our strategy is to model the MW halo as an NFW profile in the absence of baryons which is subsequently modified by the Galactic baryonic distribution. For this we select from the three simulation suites those systems whose density profile in the DMO version is well described by an NFW profile – this represents most of the haloes in our sample (78 per cent). Some haloes are not in equilibrium, typically because of transient events such as mergers (e.g. see Neto et al. 2007); including such haloes would misrepresent the long-term relation between the DM distributions in the DMO and hydrodynamics simulations so we do not consider them further.

We proceed by fitting an NFW profile (Navarro et al. 1996, 1997) given by:

$$\rho(r) = \frac{\rho_0 R_s^3}{r(r + R_s)^2} \tag{7}$$

$$\equiv \frac{M_{200}}{4\pi R_{200}^3} \frac{c^3}{\ln(1+c) - \frac{c}{1+c}} \frac{R_s^3}{r(r + \frac{R_{200}}{c})^2}, \tag{8}$$

where ρ_0 is the characteristic density, $R_s = R_{200}/c$ is the scale radius, and c is the halo concentration. If we know the halo mass, then the NFW profile is determined by a single parameter, which can be taken as the concentration (see equation 8).

To find the best-fitting NFW profiles, we minimize

$$\sigma_{\text{fit}} = \frac{1}{N-1} \sum_{i=1}^{N} \left(\log \rho_i - \log \rho_{\text{NFW};i} \right)^2, \tag{9}$$

where the sum is over all the N radial bins used for the fit. As argued in previous studies (e.g. Neto et al. 2007; Schaller et al. 2015), we limit the fits to the radial range $[0.05, 1]R_{200}$. We perform the fitting using a single free parameter: the halo concentration, c. We have also tested two-parameter fits, in which the total mass, M_{200}, is also allowed to vary and found very similar results.

Our final sample is composed of only the haloes whose DMO version is well described by an NFW profile, which we determine by requiring that the error in the fit (see equation 9) be smaller than 8×10^{-3}. Due to slight stochastic and dynamical differences between the DMO and full physics simulations, mergers can take place at slightly different times in matched haloes in the two simulations. To ensure that we only consider haloes in near equilibrium in the hydrodynamic version we apply the Neto et al. (2007) criterion to further remove any systems in which the subhalo mass fraction is higher than 10 per cent. Our final sample consist of 33 medium-resolution and 5 high-resolution Auriga haloes, 16 medium-resolution, and 6 high-resolution APOSTLE haloes, and 27 EAGLE_recal haloes.

We account for the limited resolution of the simulations by considering only regions at $r > 2r_{\text{conv}}$, where r_{conv} is the convergence radius from Ludlow, Schaye & Bower (2019a, see also Power et al. 2003). We extend the range to twice the convergence radius because in hydrodynamics simulations the difference in the Masses of the DM and star particles enhances artificial two-body scattering (for more details see Ludlow et al. 2019b).

The rotation curves for our sample of 87 simulated galaxies are shown in Fig. 1, where they are compared to the measurement of the MW circular velocity by Eilers et al. (2019). The rotation curve is measured in the plane of the stellar disc, which is identified with the plane perpendicular to the angular momentum of the stellar distribution within 10 kpc from the centre of the galaxy. The velocity is calculated as $V_{\text{circ}}^2 = R \, d\Phi_{\text{tot}}/dR$, where Φ_{tot} is the total gravitational potential and R is the radial distance in the plane of the disc. The rotation curve of each simulated galaxy is coloured according to the galaxy stellar mass contained within 10 kpc from its centre. Our simulated systems show a diversity of rotation curves, with maximum values ranging from ~ 140 to $\sim 300 \, \text{km s}^{-1}$. The low stellar mass galaxies have low circular velocities that tend to increase with radius, indicating that their dynamics are dominated by the DM component. In contrast, the galaxies with large stellar masses have rotation curves that tend to decrease with radial distance.

The circular velocities of our simulated galaxies span a range of values around the measurements for the MW. Some of them are,
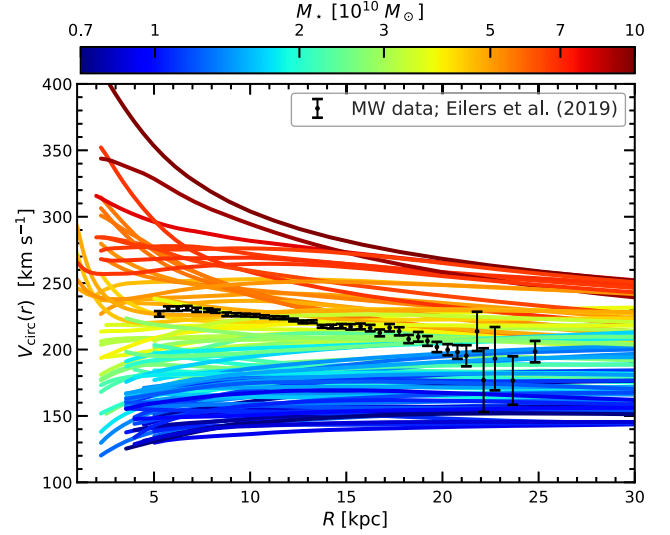

Figure 1. Rotation curves for the 87 simulated galaxies used in this work. Each line corresponds to one system. The lines are coloured according to the stellar mass of the galaxy (see legend at the top). The black symbols with error bars show the Eilers et al. (2019) determination of the MW rotation curve. The error bars correspond to the statistical uncertainties associated with the Eilers et al. measurement. For $R > 20$ kpc the MW measurement has large (~ 10 per cent or higher) systematic uncertainties and thus should be interpreted with care.

in fact, quite close matches to the MW. In particular, the rotation curves of simulated galaxies with $M_\star \sim 4 \times 10^{10} \, \text{M}_\odot$ match the data well at $R < 20$ kpc (at farther distances the measurements have large systematic uncertainties that are not shown) in terms of both absolute value as well as radial gradient. This stellar mass is in good agreement with estimates for the MW (e.g. Bovy & Rix 2013; McMillan 2017, and Section 5); thus some of our simulated galaxies can be regarded as close analogues of our galaxy.

3.3 DM halo profile in the presence of baryons

To study the halo profile in the hydrodynamic simulations, we start by comparing the enclosed DM mass at different radial distances between the hydrodynamics run, $M_{\text{DM}}(<r)$, and the DMO run, $M_{\text{DM}}^{\text{DMO}}(<r)$. In the DMO case all the corresponding mass is associated with a DM particle but, in reality, each particle should be thought of as containing a fraction, f_{bar}, of baryons and a fraction $1 - f_{\text{bar}}$ of DM, where $f_{\text{bar}} = \Omega_b/\Omega_m$ is the cosmological baryon fraction. This implies that the DM mass for the DMO run is given by $(1 - f_{\text{bar}})M_{\text{tot}}^{\text{DMO}}$, where $M_{\text{tot}}^{\text{DMO}}$ denotes the total mass in the DMO simulation.

Fig. 2 shows the radial dependence of the ratio, $\eta_{\text{DM}} = M_{\text{DM}}(<r)/M_{\text{DM}}^{\text{DMO}}(<r)$, between the enclosed DM mass in the hydrodynamics and in the DMO simulations. Each halo in our three simulation suites is shown as a curve whose colour reflects the stellar mass, $M_\star$, of the central galaxy. We find that in all cases the inner $r < 10$ kpc halo is contracted (i.e. $\eta_{\text{DM}} > 1$), which implies that the condensation of baryons at the centre of their haloes leads to an increase in the enclosed DM mass too. The increase is largest for the most massive central galaxies. Farther from the halo centre we find that some systems still have contracted DM haloes, i.e. $\eta_{\text{DM}} > 1$, while others (especially the ones with low $M_\star$) have $\eta_{\text{DM}} < 1$, that is less enclosed DM than in the DMO case. These results are in good agreement with other hydrodynamics simulations, such
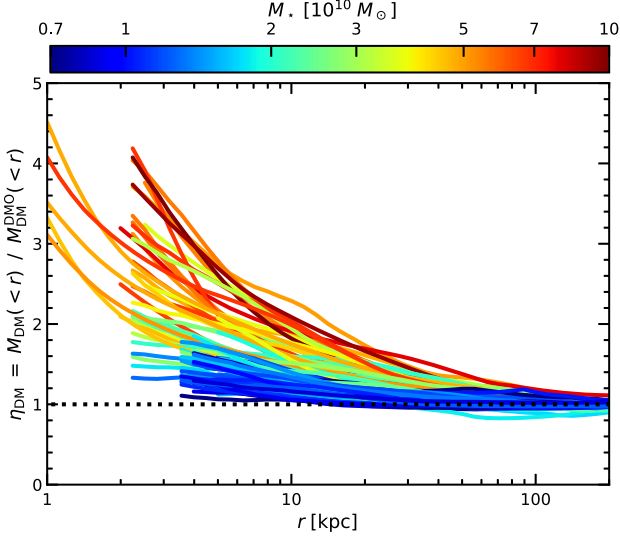
Figure 2. The radial dependence of the ratio, η_{DM}, between the enclosed DM mass in the full physics run, $M_{DM}(<r)$, and in the DMO only run, $M_{DM}^{DMO}(<r)$. Each line corresponds to a galaxy inside a MW-mass halo from either the Auriga, APOSTLE or EAGLE_recal hydrodynamical simulations. The lines are coloured according to the stellar mass of the central galaxy (see colour bar at the top of the panel). We show results only for distances larger than that twice the Power et al. (2003) radius (see the main text). We show results for multiple resolutions, with the highest resolution systems corresponding to the curves that go down to the lowest r values.

as NIHAO (Dutton et al. 2016) and IllustrisTNG (Lovell et al. 2018), which also show that, on average, the DM halo is contracted and the amplitude of the contraction varies among different systems.

The response of the DM halo to the assembly of its galaxy can be predicted to good approximation using the adiabatic contraction method in which the DM distribution is assumed to have the same action integrals in the hydrodynamic run as in the DMO case (Sellwood & McGaugh 2005; Callingham et al. 2020, the latter study has explicitly tested this prediction with the Auriga galaxies). However, as we discussed in the Introduction, this is a rather involved and needlessly complicated process. Other simpler adiabatic contraction approximations, such as those used by Blumenthal et al. (1986) and Gnedin et al. (2004), tend systematically to under- or overpredict the halo contraction (e.g. Abadi et al. 2010; Duffy et al. 2010; Pedrosa, Tissera & Scannapieco 2010; Dutton et al. 2016; Artale et al. 2019). In the following, we provide a new description of how the DM halo responds to galaxy formation processes, that combines the simplicity of approximate methods with the accuracy of more involved ones.

We have studied the change in the DM profile as a function of the change in gravitational potential at fixed r between the DMO and the hydrodynamic simulations, which is given by $\chi_{tot} = M_{tot}^{DMO}(<r)/M_{tot}(<r)$ (the mass with a DMO prefix is for the DMO only runs and the one without a prefix is for the hydrodynamics runs). We have found that the ratio of the enclosed DM mass, $\eta_{DM} = M_{DM}(<r)/M_{DM}^{DMO}(<r)$, at a given distance, r, is highly correlated with χ_{tot}. This relation is shown in Fig. 3, where each data point corresponds to the pair of (χ_{tot}, η_{DM}) values for each galaxy measured at different distances from the centre. The tight correlation of the (χ_{tot}, η_{DM}) values is especially surprising since the same η_{DM} value can correspond to measurements at very different physical radii, depending on the stellar mass of a galaxy.
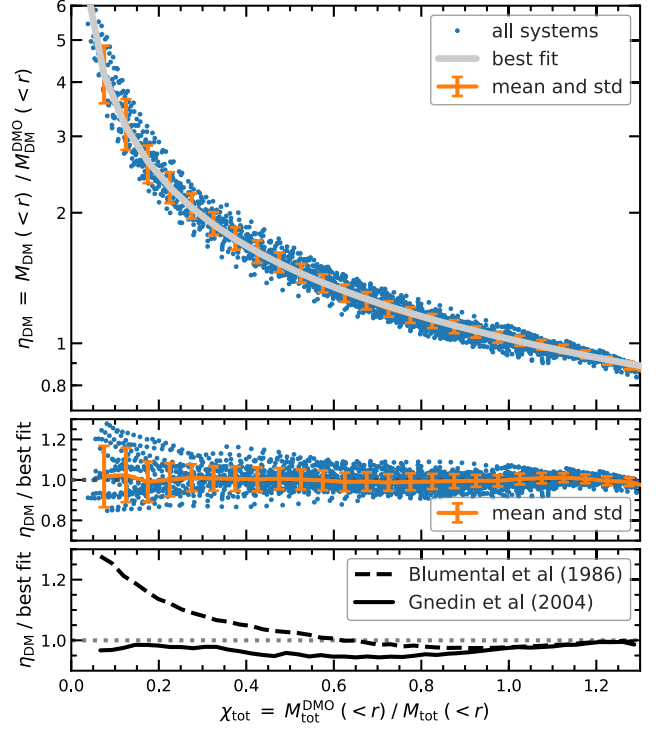

Figure 3. The DM halo response to the assembly of its central galaxy. Top panel: the ratio of the enclosed DM mass, $\eta_{DM} = M_{DM}/M_{DM}^{DMO}$, between the baryonic and DMO runs as a function of the ratio, $\chi_{tot} = M_{tot}^{DMO}/M_{tot}$, between the total enclosed mass in the DMO and the baryonic runs. The DM mass in the DMO run is given by $M_{DM}^{DMO} = (1 - f_{bar})M_{tot}^{DMO}$, while the total mass in the hydrodynamic run is $M_{tot} = M_{DM} + M_{bar}$. The points correspond to 87 galaxies in three suites of simulations whose mass ratios were evaluated at radial distances from 1 kpc up to R_{200}. The thick grey line corresponds to the best fitting function described by equation (10). This sits on top of the running mean, which is shown by the orange line. Centre panel: the ratio between the individual points and the best fit function. The orange line with error bars shows the running mean and 68 percentiles of the distribution. Bottom panel: comparison with the mean η_{DM} predicted by the Blumenthal et al. (1986) (dashed line) and Gnedin et al. (2004) (solid line) approximations to an adiabatically contracted halo.

Fig. 3 includes galaxies from the three simulation suites studied here: EAGLE_recal, and both the medium and high resolution runs of Auriga and APOSTLE. Although not shown, we have compared the various resolutions and found very good agreement amongst them indicating that our results do not depend on numerical resolution. We have also compared disc and spheroidal galaxies and did not find any statistically significant difference between the two morphologies.

The mean trend between χ_{tot} and η_{DM} (see solid orange line in Fig. 3) is well captured by the power-law:

$$\eta_{DM} = A \, \chi_{tot}^{B}, \tag{10}$$

with the best-fitting parameters, $A = 1.023 \pm 0.001$ and $B = -0.540 \pm 0.002$. The best fit function is shown by the grey line in the top panel of Fig. 3 which sits exactly on the median trend (i.e. the orange line). To better appreciate the quality of the fit, the centre panel of the figure shows the ratio between the individual data points and the best-fitting function. We emphasise that equation (10) has been found for galactic mass haloes, i.e. with masses $M_{200} \sim 1 \times 10^{12} \, M_{\odot}$, and remains to be checked if the same expression can describe the contraction of haloes outside this mass range.

The bottom panel of Fig. 3 compares our measured relation between χ_{tot} and η_{DM} with the predictions of two widely employed approximations for adiabatic contraction. We find that both the Blumenthal et al. (1986) and Gnedin et al. (2004) methods underestimate the DM halo contraction at high χ_{tot} values, while for $\chi_{tot} <$ 0.5 the results are mixed. In particular, for $\chi_{tot} > 0.2$ both methods are accurate at the 5 per cent level, and while this level of agreement might seem good, the systematic offset is actually larger than the typical standard deviation in the individual data points (see vertical error bars in the middle panel). Note that a 5 per cent error in the relation between χ_{tot} and η_{DM} translates into roughly a 10 per cent error in the determination of M_{DM}.

Equation (10) represents a non-linear deterministic relation between the enclosed mass ratios, χ_{tot}, and η_{DM}, which, in turn, can be expressed as a relation between $M_{DM}^{DMO}(<r)$, $M_{DM}(<r)$ and $M_{bar}(<r)$. Thus, given any two radial mass profiles, we can solve for the third. For example, we can predict the DM mass profile in the full physics simulation, $M_{DM}(<r)$, given the DM profile in the absence of baryons and the final baryonic profile. This is exactly what we are interested in doing here, since we know that $M_{DM}^{DMO}(<r)$ is well described by an NFW profile while $M_{bar}(<r)$ can be inferred from observations. These two quantities can be combined with equation (10) to predict $M_{DM}(<r)$, whose solution can be approximated as:

$$M_{DM}(<r) = M_{DM}^{DMO}(<r)\left[0.45 + 0.38\left(\eta_{bar} + 1.16\right)^{0.53}\right] . \quad (11)$$

The symbol $\eta_{bar} = M_{bar}(<r)/M_{bar}^{DMO}(<r)$ denotes the ratio between the enclosed baryonic masses in the hydrodynamics and the DMO runs, where $M_{bar}^{DMO} = f_{bar}M_{tot}^{DMO}$.

We finish this section by testing how well equation (11) reproduces the contraction of the DM halo. For each halo in our sample, we take the $M_{bar}(<r)$ profile from the hydrodynamics simulation and take $M_{DM}^{DMO}(<r)$ as the best fitting NFW profile to the DM distribution in the DMO run. We find the predicted DM mass, $M_{DM}^{pred}(<r)$, at each r, which we then compare against the actual DM mass distribution measured in the hydrodynamic run, $M_{DM}(<r)$. The results are shown in top panel of Fig. 4. The mean ratio of predicted and measured DM masses is very close to one at all r, showing that the method is unbiased. Nonetheless, individual haloes can deviate from the mean prediction since the size of the contraction is weakly dependent on the assembly history of the system (e.g. Abadi et al. 2010; Artale et al. 2019). The halo contraction can be best predicted at large radial distances, where the halo-to-halo variation is ∼5 per cent and is dominated by deviations of the DMO halo from an NFW profile. In the inner parts, individual haloes can deviate more from our prediction, but still at a reasonably low level, with a halo-to-halo scatter of 7 per cent at the Sun's position and 13 per cent at 2 kpc.

The bottom panel of Fig. 4 addresses a crucial question: do the predictions depend on the galaxy formation model? To find the answer, we test the accuracy of the method separately for the Auriga, APOSTLE and EAGLE_recal samples. For each of the three simulations we show the mean and the dispersion of the ratio between predicted and measured DM masses as a function of radial distance. We find very good agreement between APOSTLE and EAGLE_recal, which was to be expected since these two simulations use similar galaxy formation models. We also find good agreement with the Auriga sample: although this is systematically higher, the difference is smaller than the scatter amongst individual systems. The response of the DM halo to the baryonic component depends on the galaxy assembly history (e.g. Duffy et al. 2010; Dutton et al. 2016; Artale et al. 2019); the good agreement between the halo
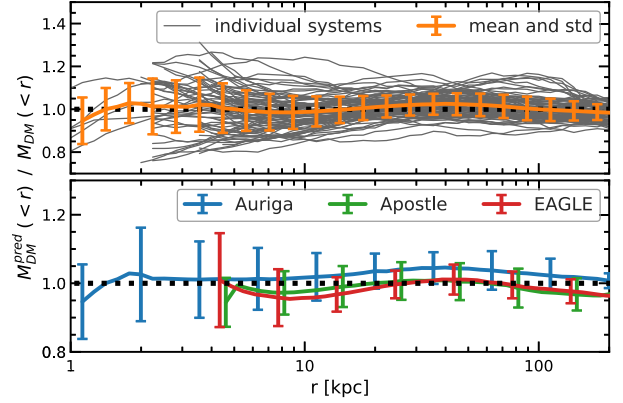

Figure 4. Test of the extent to which our method can recover the contracted DM distribution as a function of radial distance. The vertical axis shows the ratio between the predicted enclosed DM mass, $M_{DM}^{pred}(<r)$, and the value measured in the hydrodynamics simulation, $M_{DM}(<r)$. The predicted DM mass is calculated from an NFW fit to the corresponding halo in the DMO run. The top panel shows individual galaxies (grey lines) as well as the mean and the 68 percentiles of the distribution (thick orange line). The bottom panel compares the mean and the 68 percentiles for galaxies in each of the three simulation suites used here: Auriga (blue line), APOSTLE (green line), and EAGLE_recal (red line). Our method for inferring the DM halo contraction is unbiased and works equally well for all three simulations. The halo-to-halo scatter grows from 5 per cent at $r = 100$ kpc, to 7 per cent at $r = 10$ kpc and reaches 13 per cent at $r = 2$ kpc.

contraction predictions in our three simulations suites reflects the fact that these simulations have galaxy growth histories that match observations (see Furlong et al. 2015, and discussion therein).

4 THE CONTRACTION OF THE MW'S HALO

Shortly, in Section 5, we will fit the MW rotation curve to infer the baryonic and DM mass profiles of our galaxy. Before doing so, in this section, we present a brief analysis of how important is the DM halo contraction given the baryonic distribution in the MW. Then, in the second part, we study biases and systematic errors that arise from not accounting for this contraction. In particular, we compare the MW total mass and DM halo concentration inferred assuming that the MW halo is well described by an NFW profile – the usual approach in the literature – with the values inferred when the DM halo contraction is taken into account.

To make the results of this section as relevant as possible to our actual Galaxy, we use the best-fitting baryonic mass profile for the MW which we infer in Section 5. This is given in terms of the MW baryonic components described in Section 2 with the parameter values given in Table 1 and in the fifth column (labelled 'best fitting values for contracted halo') of Table 2. The enclosed MW baryonic mass as a function of radial distance is shown by the black line in Fig. 5.

4.1 Galactic halo contraction

Both the mass and the concentration of the Galactic halo are uncertain, so we exemplify the DM halo contraction for a range of halo masses and concentrations. In all cases we assume that, in the absence of baryons, the MW DM halo is well described by an NFW profile (see the discussion in the Introduction) which,
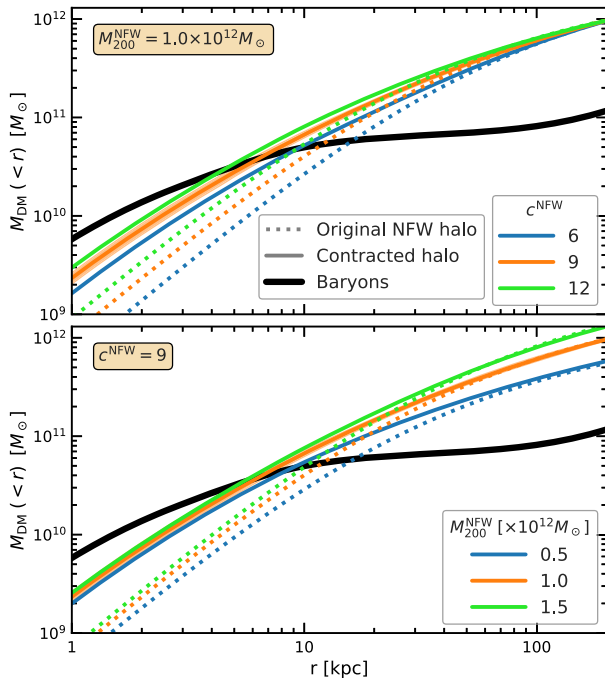
Figure 5. The radial enclosed mass profile of NFW haloes (dotted lines) and their contracted counterparts (solid lines) given the MW baryonic distribution. The solid black line shows the Galactic enclosed baryonic mass profile. The top panel corresponds to initial NFW haloes of the same mass but different concentrations. The bottom panel corresponds to haloes with the same concentration but different masses.
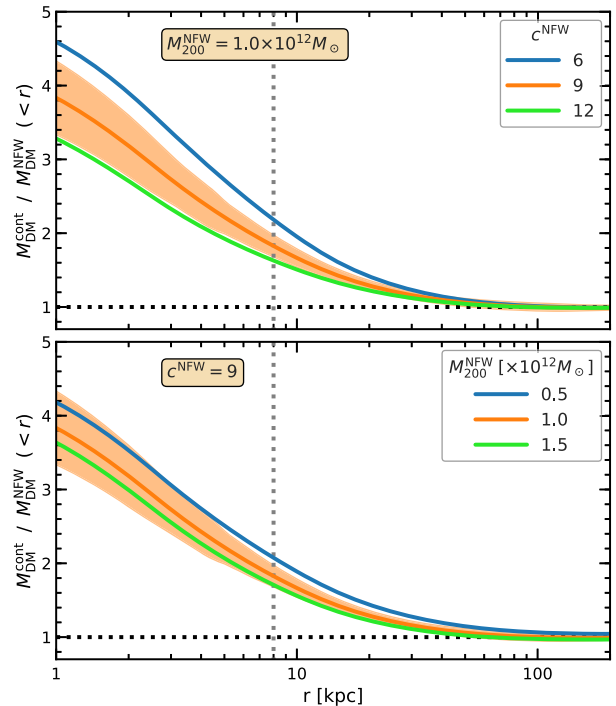

Figure 6. The contraction of the Galactic DM halo for different halo masses and concentrations. The Y-axis is the ratio of the enclosed DM mass in the contracted halo to that in the original NFW halo. In all cases the MW halo, in the absence of baryons, is described by an NFW profile of mass, M_{200}, and concentration, c^{NFW}, that is then contracted according to the Galactic baryonic distribution. The top panel shows haloes with mass, $M_{200} = 1 \times 10^{12}$ M$_\odot$, and concentrations ranging from 5 to 11. The bottom panels shows haloes with concentration, $c^{NFW} = 9$, and masses ranging from 0.5 to 1.5×10^{12} M$_\odot$. The orange shaded region shows the 68 percentile halo-to-halo scatter in the predictions as determined in Fig. 4 (the scatter is shown only for the orange line). The vertical dotted line shows the Sun's position, $r_\odot = 8.2$ kpc.

in the presence of baryons, is contracted according to the relation introduced in Section 3.3.

Fig. 6 shows the increase in the enclosed DM mass due to the presence of baryons at the centre. For example, if the MW resides in a 1×10^{12} M$_\odot$ halo with the average NFW concentration for this mass, $c^{NFW} = 9$ (orange line in top panel), then the baryons lead to an increase in the enclosed mass at distances $r < 50$ kpc. While the increase is largest for small r, it is still significant at larger distances too, as for example the Sun's orbit encloses twice as much DM, and a 20 kpc radius 30 per cent more DM than the uncontracted halo. The shaded region around the orange line shows the typical halo-to-halo scatter (see Fig. 4) and illustrates that we can predict, with a high degree of confidence, that the Galactic halo is contracted.

At distances, $r > 100$ kpc, we notice a small (barely visible) decrease in the enclosed mass of the contracted halo, which reflects a slight expansion of the outer halo. This is caused by the fact that at those distances the enclosed baryonic mass is below the universal baryonic fraction for the given halo mass and thus the halo experiences the opposite effect from a contraction: it expands, but only slightly. Note that while our MW model does include a CGM component, this is not massive enough to bring up the halo baryonic content to the cosmic baryon fraction. For example, if the Galactic DM halo mass is 1.0×10^{12} M$_\odot$, then within R_{200} the baryon fraction is 73 per cent of the cosmic value.

The top panel of Fig. 6 also shows the contraction of equal mass haloes of different concentrations. The blue and green curves correspond to concentrations in the absence of baryons of $c^{NFW} = 5$ and 11, respectively, which, while falling in the tails of the c^{NFW} distribution, are not very extreme values. The plot illustrates that the size of the halo contraction depends sensitively on the halo

concentration, with lower concentration haloes experiencing greater contraction.

The bottom panel of Fig. 6 shows that the size of the contraction also depends on halo mass, but to a lesser extent than on halo concentration. In this case, the blue and green curves correspond to DM halo masses of $M_{200} = 0.5 \times$ and 1.5×10^{12} M$_\odot$, respectively. We find that for the same baryonic distribution, lower mass haloes contract more.

To understand why the amplitude of the contraction depends on both halo mass and concentration it is useful to compare the radial profile of the DM with that of the baryons. This is shown in Fig. 5 where the thick black line shows the enclosed baryonic mass, and the various coloured lines show the enclosed DM mass profile for a range of halo masses and concentrations. The dotted lines correspond to the original (i.e. uncontracted) NFW profiles while the solid lines show the contracted DM distributions. We find that in the inner region, where baryons dominate, the contraction leads to DM profiles that are much more similar to one another than to the original NFW distributions. This implies that the baryons are the main factor that determines the contracted DM distribution, with the original DM distribution having a secondary effect. As a result, lower mass or lower concentration haloes, which have less mass in their inner regions, must contract more than higher mass or higher concentration haloes.
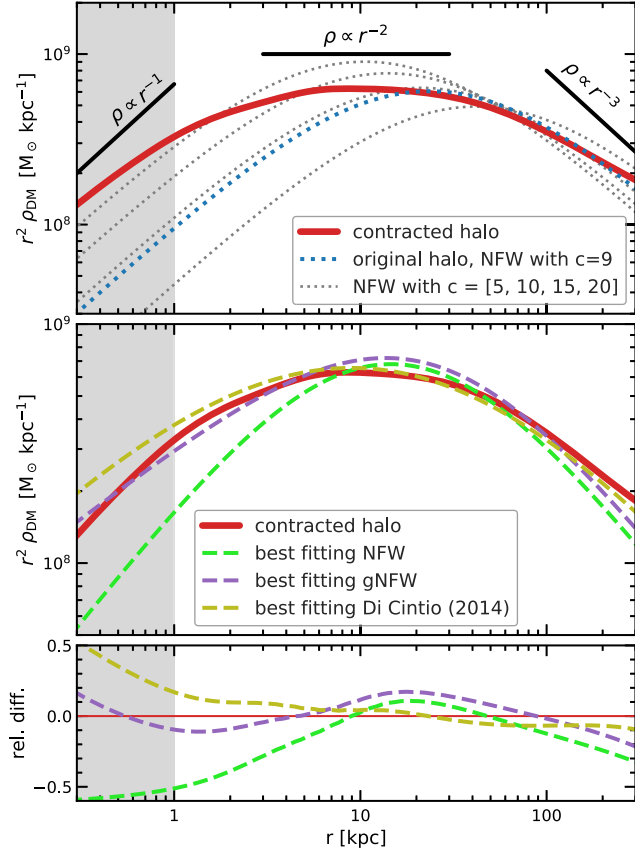
Figure 7. Top panel: the density profile of an NFW halo (blue dotted curve) of mass, $M_{200} = 1 \times 10^{12} \, \mathrm{M_\odot}$, and concentration, $c^{\mathrm{NFW}} = 9$, and its contracted counterpart (solid red line) given the MW baryonic distribution. This halo profile is roughly the same as the best fitting Galactic DM halo inferred in Section 5. The grey dotted lines show NFW profiles for the same halo mass but different concentrations. Middle panel: the best fits to the contracted Galactic DM halo (solid red line) with an NFW (green dashed line), generalized NFW (purple dashed line) and Di Cintio et al. (2014, yellow dashed line) profiles. Bottom panel: the relative difference, $\rho_{\mathrm{best \, fit}}/\rho_{\mathrm{contracted}} - 1$, between the contracted halo and the three best fitting profiles shown in the middle panel. The grey shaded region corresponds to $r < 1 \, \mathrm{kpc}$, the regime within which halo contraction has been extrapolated to radii smaller than those for which we have tested our method.

We now investigate if the profile of the contracted halo can be described by a simple parametric form, such as an NFW profile or more flexible generalizations. We illustrate this assuming that the MW galaxy formed in a halo which, in the absence of baryons, is described by an NFW profile with mass, $M_{200} = 1 \times 10^{12} \, \mathrm{M_\odot}$, and concentration, $c^{\mathrm{NFW}} = 9$. As we shall see later in Section 5, this halo profile is very close to the best fitting model for the pre-contracted Galactic halo. The original NFW halo, as well as its contracted version, are shown in the top panel of Fig. 7 with blue dotted and red solid lines, respectively. The various grey dotted lines show NFW profiles for a halo with the same mass but different concentrations and clearly illustrate that the contracted NFW halo profile is not of the NFW form.

The middle panel of Fig. 7 shows the best-fitting NFW profile, in which both the concentration and the mass are left as free parameters, to the contracted halo. Since the contracted halo does not follow an NFW profile, the resulting best-fitting NFW function depends somewhat on the radial range use for the fit. Here, we fit

over the radial range $5 \le r/\mathrm{kpc} \le 200$ (the fit is qualitatively similar if we use different reasonable radial ranges), to obtain the green dashed line in the two bottom panels. The best-fitting NFW form shows large deviations from the contracted halo profile, ~ 20 per cent and even larger, indicating that an NFW profile is a poor description of a contracted halo profile. These differences are best illustrated in the bottom panel of Fig. 7, which shows the relative difference between the best-fitting profiles and the density of the contracted halo.

We have also tested a more flexible function, the so-called generalized NFW (gNFW) profile, given by:

$$\rho(r) = \frac{\rho_0}{r^\gamma (r + R_s)^{3-\gamma}}, \tag{12}$$

which, has a third parameter, γ, in addition to the two parameters, R_s and ρ_0, of the NFW profile. We have fitted the gNFW profile over the same radial range as the NFW profile to obtain the purple dashed line shown in the middle and bottom panels of Fig. 7. The gNFW parametrization does better at matching the contracted profile in the region $r < 5 \, \mathrm{kpc}$, even though that region was not used in the fit; however, it still performs poorly at $r > 8 \, \mathrm{kpc}$. In particular, the gNFW best fit still shows a ~ 20 per cent deviation from the contracted profile in the radial range $8 \, \mathrm{kpc} < r < 20 \, \mathrm{kpc}$. This is a concern because this radial range is the sweet-spot between the range for which the MW rotation curve is least uncertain and the radii at which the DM halo becomes dominant, so that the data in this intermediate region have the potential to best constrain the Galactic DM halo.

The inability of an NFW or gNFW function (or other functions such as an Einasto profile) to describe the contracted profile is a direct manifestation of the fact that in the radial range, $5 \, \mathrm{kpc} < r < 30 \, \mathrm{kpc}$, the DM density varies roughly as $\rho_{\mathrm{DM}} \propto r^{-2}$ (i.e. $r^2 \rho_{\mathrm{DM}}$ is flat – see black line in the top panel of Fig. 7). The gNFW and Einasto profiles have a range where $\rho_{\mathrm{DM}} \propto r^{-2}$, but this is typically limited to a very narrow interval in r, while we predict that the contracted Galactic DM halo should show this behaviour over a much wider radial range. More general profiles, such as the Schaller et al. (2015) or the Dekel et al. (2017) ones, have more free parameters and potentially can provide a better match to the contracted halo profile. However, in practice, their flexibility is also a limitation since the observational data are not good enough to provide interesting constraints on the larger number of free parameters (e.g. when fitting the MW rotation curve, Karukes et al. 2019b found that the R_s and γ parameters of the gNFW models are highly degenerate). As we shall discuss in Section 5, inferences based on current MW data already results in 20 per cent uncertainties for 2-parameter DM halo models and these are likely to be even higher for models with more free parameters.

Some previous works have adopted profiles with several free parameters and fitted them to the DM density profiles in hydrodynamical simulations. One example is the study of Di Cintio et al. (2014), who found that a five parameter profile of the form,

$$\rho(r) = \frac{\rho_0}{\left(\frac{r}{R_s}\right)^\gamma \left[1 + \left(\frac{r}{R_s}\right)^\alpha\right]^{(\beta-\gamma)/\alpha}}, \tag{13}$$

provides a good description of the DM halo profile in their hydrodynamic simulations for a wide range of halo masses. In particular, these authors found that the α, β, and γ parameters in equation (13) depend only on the stellar-to-halo mass ratio, and thus leaving only two free parameters, ρ_0 and R_s. Using the Di Cintio et al. (2014) predicted values for α, β, and γ, we fitted the contracted NFW halo distribution in Fig. 7 using equation (13) with two free parameters, ρ_0 and R_s. The resulting best-fitting function

is shown in Fig. 7 by the yellow dashed line. This functional form captures the contracted halo profile reasonably well, with typical errors of 10 per cent or less. However, these errors are still larger than the typical uncertainties in the MW rotation curve and could lead to systematic biases in the inferred halo mass or concentration.

4.2 Biases in inferred halo properties

We saw in the previous subsection that the settling of baryons at the centre of a DM halo causes the halo to contract and, as a result, the density profile no longer follows the NFW form. However, many previous studies have modelled the Galactic halo as an NFW profile, which raises an important question: what are the biases in the inferred halo parameters that result when fitting an NFW halo to the observational data? To answer this question we proceed to study how the inferred DM halo mass and concentration differ when the data are fit with either a contracted NFW halo or an uncontracted NFW profile.

We first infer a DM halo mass and concentration by fitting the enclosed mass at two different distances from the Galactic Centre, the Sun's position, $r = 8$ kpc, and $r = 20$ kpc. We study the enclosed mass at two radii because the contraction of the halo becomes less important with increasing distance from the Galactic Centre and thus systematic differences between a contracted and an NFW halo are distance dependent. For simplicity, we assume that there is no uncertainty in the profile of the baryonic component, and infer the DM halo properties: total mass and concentration (for the contracted halo, the concentration corresponds to the value before contraction). The resulting 68 and 95 per cent confidence limits for M_{200}^{DM} and c^{NFW} are shown in Fig. 8. To calculate the enclosed masses we used the Eilers et al. (2019) circular velocity measurement, $V_{circ}(r = 8$ kpc$) = (230 \pm 5)$ km s^{-1}, and the enclosed total mass measurement of Posti & Helmi (2019), $M^{tot}(<r = 20$ kpc$) = (1.91 \pm 0.18) \times 10^{11}$ M$_\odot$.

Using a single mass measurement results in a degeneracy between the inferred halo mass and concentration since different (M_{200}^{DM}, c^{NFW}) pairs can produce the same enclosed DM mass, as may be seen from the coloured shaded regions in Fig. 8. More interestingly, the figure shows that modelling the DM halo as an NFW or a contracted profile results in very different estimates of the halo mass and concentration. The difference is especially striking for the estimates at $r = 8$ kpc (top panel in Fig. 8), where we find that even the 95 per cent confidence limits for the two models do not overlap. At larger distances, such as at $r = 20$ kpc shown in the bottom panel of Fig. 8, the baryons lead to a smaller contraction of the DM halo and the two model estimates are in closer agreement, but still do not have overlapping 68 per cent confidence limits.

The (M_{200}^{DM}, c^{NFW}) confidence regions can be combined with other measurements or theoretical priors to narrow the uncertainty regions. For example, the (roughly) horizontal dashed line and its associated grey-shaded region show the halo mass–concentration relation from DM-only cosmological simulations (Hellwing et al. 2016; this is very similar to other recent mass–concentration relations, as may be seen from Fig. 5 of that paper). Using the relation as a prior, we can estimate the DM mass of the Galactic halo. Doing so for the contracted NFW halo model results in a consistent estimate of $M_{200}^{DM} \sim 1 \times 10^{12}$ M$_\odot$ for both $r = 8$ and 20 kpc, which is in good agreement with the recent estimate by Callingham et al. (2019, vertical dashed line). In contrast, the NFW halo model prefers a very high DM mass at $r = 8$ kpc, $M_{200}^{DM} \sim 1 \times 10^{13}$ M$_\odot$, and a much lower mass, $\sim 1.5 \times 10^{12}$ M$_\odot$, at $r = 20$ kpc.
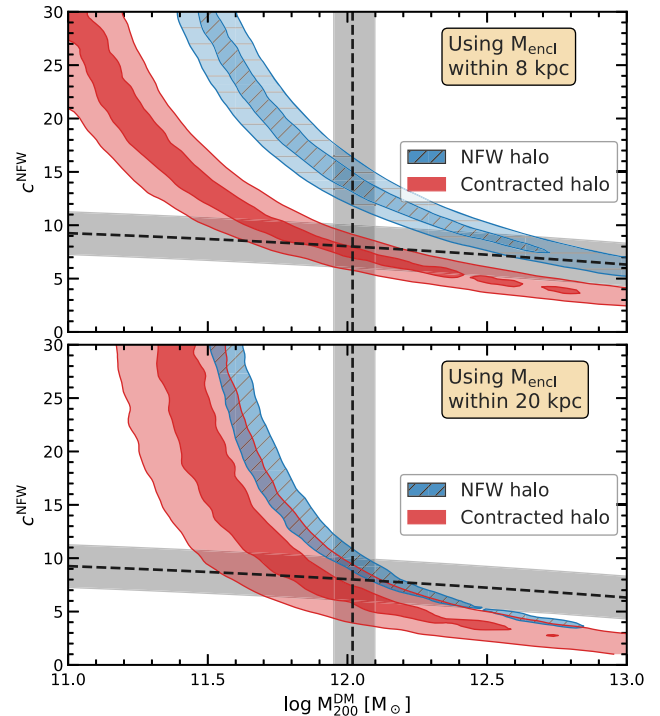

Figure 8. Constraints on the mass and concentration of the MW DM halo inferred from the enclosed mass within 8 kpc (top panel) and within 20 kpc (bottom panel). The blue shaded region corresponds to modelling the halo as an NFW profile. The red shaded region corresponds to modelling the halo as an NFW profile that has been contracted by the MW baryonic distribution – in this case the concentration corresponds to the original (uncontracted) halo. The dark and lighter colours show the 68 and 95 percentile confidence regions, respectively. For clarity, for the NFW case in the bottom panel, we show only the 68 percentile confidence region. The vertical dashed line and the associated grey region show the Callingham et al. (2019) MW DM halo mass estimate and its 68 percentile confidence region. The approximately horizontal dashed line and its associated grey region show the median and standard deviation of the halo mass–concentration relation (Hellwing et al. 2016).

More interesting is to combine the contours in Fig. 8 with other DM mass estimates to infer the concentration of the Galactic DM halo. We illustrate this by showing the Callingham et al. (2019) DM mass estimate and its associated 68 per cent confidence interval, which are shown in the figure as the vertical dashed line and associated grey shaded region. The contracted halo model predicts that the MW has an (uncontracted) concentration, $c^{NFW} \sim 8$, which is typical of a 1×10^{12} M$_\odot$ ΛCDM halo – this can be inferred from the fact that the vertical and horizontal dashed lines intersect inside the dark shaded region in both panels in the figure. In contrast, the inferred concentration for the NFW halo model is very different for the two radial measurements shown in Fig. 8 and is systematically higher than the theoretical ΛCDM prediction. Thus, incorrectly modelling the MW halo using an NFW profile can lead to a large overestimate of its concentration.

A complementary method for constraining the Galactic DM halo mass is by measuring the escape velocity, V_{esc}, which, despite its name, is not the velocity needed to reach infinite distance with zero speed. Deason et al. (2019a) have shown that the escape velocity characterizes the difference in gravitational potential between the position where V_{esc} is measured and the potential at a distance $2R_{200}$ from the halo centre. The potential depends on the mass
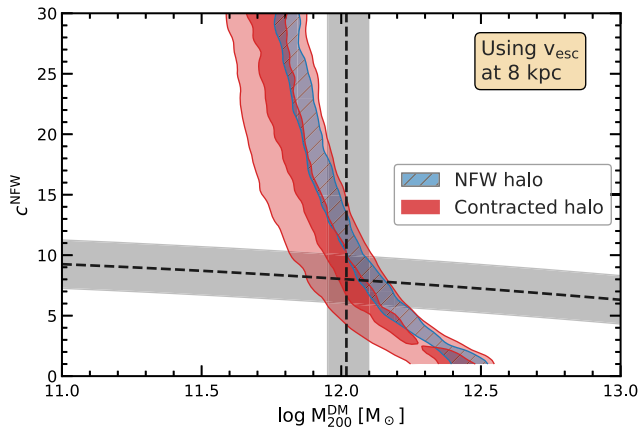
Figure 9. Constraints on the mass and concentration of the MW DM halo inferred from the escape velocity measurement of Deason et al. (2019a). The blue shaded region shows the 68 percentile confidence region when modelling the halo as an NFW profile. The red shaded regions show the 68 and 95 percentile contours when taking into account the contraction of the Galactic DM halo – in this case the concentration corresponds to the value before applying the baryonic contraction. The dashed lines and grey shaded regions are as in Fig. 8.

profile of the halo up to $2R_{200}$ and thus modelling the DM halo as a contracted or an NFW profile can introduce different biases from those present in enclosed mass measurements. These are studied in Fig. 9, where we show the inferred DM halo properties using the recent measurement of the escape velocity at the position of the Sun, $V_{esc} = (528 \pm 25)\,\mathrm{km\,s^{-1}}$, by Deason et al. (2019a).

Fig. 9 shows that using an NFW profile instead of a contracted NFW halo also leads to biases in modelling the escape velocity. Given the current uncertainty in the V_{esc} measurement, the 68 per cent confidence regions for the two models barely overlap; however this will not be the case with for future large data sets. Compared to Fig. 8, the escape velocity predictions are less affected by using the incorrect NFW profile since much of the escape velocity is determined by the mass at large Galactocentric radii where both the contracted halo and the NFW profile are very similar. Nonetheless, there are still differences between these two profiles in the inner region of the halo, which explains why the incorrect NFW model prefers systematically higher concentrations than the contracted halo model.

5 A TOTAL MASS MODEL FOR THE MW

In this section we describe the data and fitting procedure used to determine the baryonic and DM mass profiles of our galaxy. We perform the analysis in the same spirit as Dehnen & Binney (1998, see also Klypin, Zhao & Somerville 2002; Weber & de Boer 2010; McMillan 2011; Bovy et al. 2012; Kafle et al. 2014; McMillan 2017), that is, we estimate the best-fitting MW mass model by varying several parameters that encode our ignorance about stellar and DM distributions of our galaxy. For the DM, we fit two models: a contracted NFW halo, which is motivated by the predictions of hydrodynamical simulations (see Section 3), and a pure NFW profile, which is one of the most commonly used profiles in previous studies.
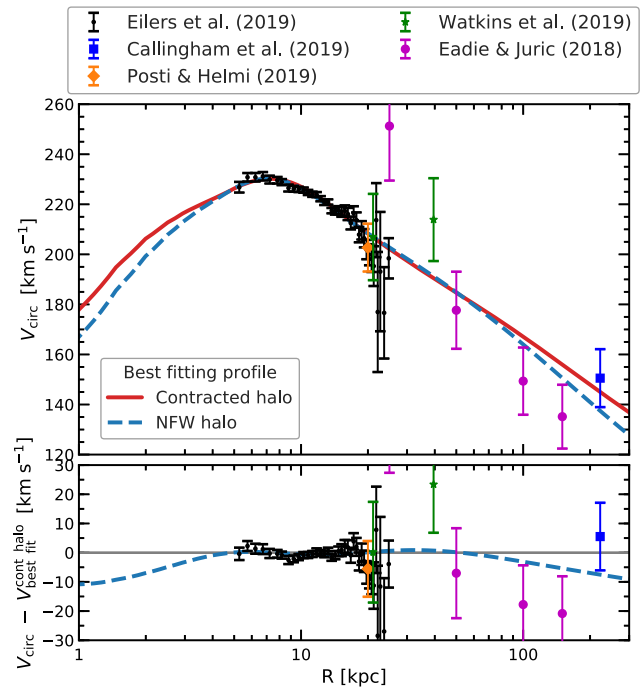
Figure 10. Top panel: MW Galactic rotation curve (symbols with error bars) as a function of radial distance. The solid red line is the best fitting MW mass model assuming a contracted DM NFW halo. The dashed blue line the best-fitting MW mass model assuming no contraction, i.e. that the DM halo follows an NFW profile. Both models were fitted only to the Eilers et al. (2019) and the Callingham et al. (2019) data points. Bottom panel: The difference between the data and the best fitting contracted halo model. The dashed blue line shows the difference between the NFW halo model and the contracted halo one. The two models give the same rotation curve to within $1\,\mathrm{km\,s^{-1}}$ or less in the range $5\,\mathrm{kpc} < r < 60\,\mathrm{kpc}$.

5.1 Data

The main constraining power of our model comes from the Eilers et al. (2019) circular velocity data (black data points in Fig. 10). These data are inferred from axisymmetric Jeans modelling of the 6D phase space distribution of more than 23 000 red giant stars with precise parallax measurements. The stellar positions and velocities come from a compilation of *Gaia* DR2 measurements, combined with improved parallax determinations from APOGEE DR14 spectra and photometric information from WISE, 2MASS, and *Gaia* (for details see Hogg, Eilers & Rix 2019).

The Eilers et al. rotation curve provides good constraints in the inner parts of the MW system; however this does not fully break up the degeneracy between DM halo mass and concentration. To deal with this, we make use of the total mass estimate of Callingham et al. (2019), $M_{200,\mathrm{MW}}^{\mathrm{total}} = (1.17 \pm 0.18) \times 10^{12}\,\mathrm{M_\odot}$. These authors infer the mass by comparing the observed energy and angular momentum distribution of the classical MW satellites with the predictions of hydrodynamical simulations. While there are many Galactic mass estimates (e.g. see the compilations in Wang et al. 2015; Callingham et al. 2019), we choose the Callingham et al. result since it has several advantages compared to other studies: (i) the method had been thoroughly tested with multiple hydrodynamic simulations, (ii) it makes use of the dynamics of satellites whose extended radial distribution directly constrains the total mass of the system, and (iii) it makes use of the latest *Gaia* DR2 proper

motion measurements for the classical dwarfs (Gaia Collaboration 2018).

To remove some of the degeneracy between the thin and thick stellar discs, we impose the prior that the ratio of the thin to thick disc densities at the Sun's position, which we take as $R_\odot = 8.122 \pm 0.031$ kpc (Gravity Collaboration 2018), is 0.12 ± 0.012. This value is derived from the analysis of MW disc stars in the SDSS data by Jurić et al. (2008).

The last measurement we consider is the value of the vertical force at 1.1 kpc above the plane at the Sun's position, which we take as (Kuijken & Gilmore 1991):

$$K_z(R_\odot) = 2\pi G \times (71 \pm 6)\, \mathrm{M}_\odot\, \mathrm{pc}^{-2}\,. \tag{14}$$

To implement this constraint, we express it as a function of the local total surface mass density, Σ, which is given by (McKee, Parravano & Hollenbach 2015):

$$\Sigma = \frac{K_z}{2\pi G} + \Delta\Sigma, \tag{15}$$

where $\Delta\Sigma$ represents a correction term for the fact that the circular velocity varies with Galactocentric radius and with the z coordinate above the disc plane. We calculate the $\Delta\Sigma$ term using equation (53) from McKee et al. (2015), combined with the Eilers et al. (2019) rotation curve to obtain $\Delta\Sigma = 9\, \mathrm{M}_\odot\, \mathrm{pc}^{-2}$.

We note that most of the constraining power comes from the Eilers et al. (2019) circular velocity data. This is due to a combination of Eilers et al. having the most data points, 38 in total, and to the fact that most of the measurements are very precise, with errors below $2\,\mathrm{km\,s}^{-1}$, corresponding to less than 1 per cent relative errors. In contrast, the vertical force measurement has an 8 per cent relative error, while the total mass estimate has a 15 per cent relative error.

5.2 The fitting procedure

To obtain the best-fitting model, we follow the Bayesian framework in which the probability of a set of parameter values, $\theta = (\log M_{200}^{\mathrm{DM}}, c^{NFW}, \rho_{0,\mathrm{bulge}}, \Sigma_{0,\mathrm{thin}}, \Sigma_{0,\mathrm{thick}}, R_{\mathrm{thin}}, R_{\mathrm{thick}})$, given the data, D, is

$$p(\theta|D) = \frac{p(D|\theta)\ p(\theta)}{p(D)}\,, \tag{16}$$

where $p(D|\theta)$ is the probability of the data given the model parameters, $p(\theta)$ is the prior distribution of parameter values, and $p(D)$ is a normalization factor. We take three Gaussian priors for $(\rho_{0,\mathrm{bulge}}, R_{\mathrm{thin}}, R_{\mathrm{thick}})$, as given in the fourth column of Table 2. For the remaining parameters we consider no prior information; that is we take a flat prior over a range much larger than the constraints inferred from the data. The likelihood, $p(D|\theta)$, is taken as the product of the likelihoods associated with each of the 41 data points described in Section 5.1, that is 38 circular velocity measurements plus one data point for each of the following: the total mass, thin to thick disc ratio, and the vertical force at the Sun's position. The circular velocity is calculated in the plane of the disc as $V_{\mathrm{circ}}^2 = R\, \mathrm{d}\Phi_{\mathrm{tot}}/\mathrm{d}R$, where Φ_{tot} is the total gravitational potential and R is the radial distance in the plane of the disc.

We are interested in obtaining a global model that fits equally well all the measurements within their uncertainties. However, when considering only the observational errors for the Eilers et al. (2019) rotation curve we find that the reduced χ^2 is close to two and that this large value is mostly driven by a couple of regions: a dip in V_{circ} at $R \sim 9$ kpc and a second one at $R \sim 20$ kpc that are several σ away from

the overall trend. Such outlying data points could drive the model away from the set of parameters that give a good global fit and force it to parameter values that better reproduce these local features, even though such features are not expected to be captured by the model. To mitigate any such problems, we introduce an additional model uncertainty, σ_{model}, such that the total uncertainty associated with a data point is given by $\sigma = \sqrt{\sigma_{\mathrm{obs}}^2 + \sigma_{\mathrm{model}}^2}$, where σ_{obs} denotes the Eilers et al. errors. We take $\sigma_{\mathrm{model}} = \mu\sigma_{\mathrm{sys}}$, where σ_{sys} is the systematic error associated with the Eilers et al. determination. In Appendix B we compare different ways of defining σ_{model} and show that our results are largely insensitive to the definition of σ_{model}. The quantity $\mu = 0.21$ denotes a weight factor whose value we have found by requiring that the reduced χ^2 should be unity (see Appendix B for details). Increasing the errors as discussed mostly affects the points in the range $R \in [8, 13]$ kpc (the ones with very small observational uncertainties of $\sim 1\,\mathrm{km\,s}^{-1}$) and leads to errors that are at most a factor of 1.5 times higher than the observational ones.

To find the best-fitting model parameters and their associated confidence intervals we employ a Markov Chain Monte Carlo (MCMC) approach using the EMCEE python module (Foreman-Mackey et al. 2013). We fit two different models for the DM halo: first, a profile that is contracted according to the baryon distribution, and, secondly, an (uncontracted) pure NFW profile.

5.3 The best-fitting models

5.3.1 The contracted halo model

The best-fitting MW rotation curve for the contracted NFW halo model is shown as the solid red line in Fig. 10. The black data points are the Eilers et al. (2019) V_{circ} data and the dark blue square is the Callingham et al. (2019) total mass estimate converted to a V_{circ} value at the halo radius, R_{200}. The other colour data points are the Posti & Helmi (2019), Watkins et al. (2019), and Eadie & Jurić (2019) estimates of the enclosed mass at various Galactocentric radii, which were converted to circular velocities as $\sqrt{GM(<r)/r}$, where G is Newton's gravitational constant and $M(<r)$ is the enclosed mass within radius, r. The latter measurements are inferred from the dynamics of globular clusters with proper motions measured by *Gaia* DR2 and several various *HST* programs (for details see Eadie & Jurić 2019).

The components of the best fitting model are shown in Fig. 11. Fig. 10 shows that the contracted NFW halo model matches well the Eilers et al. (2019) and Callingham et al. (2019) measurements, which were the ones used for the fitting procedure. The model also agrees well with the mass measurements by Posti & Helmi (2019) and Watkins et al. (2019). However, it does not match the Eadie & Jurić (2019) data particularly well, which may be due to the assumption by these authors of a power-law model for the MW potential, which is an oversimplification. For example, Eadie, Keller & Harris (2018) have tested their method against cosmological simulations and find that their estimates are often affected by systematic uncertainties that are not incorporated in their quoted error bars.

The good agreement between the model and the data can be clearly seen in the bottom panel of Fig. 10, which shows the difference between the predictions of the model and the various data points. In particular, we notice two regions where the data show systematic deviations from the model. First, at $r \sim 9$ kpc, the data show a small, but statistically significant dip compared to the model. This dip is probably due to localized irregularities in the kinematics of our galaxy since it is also present when comparing
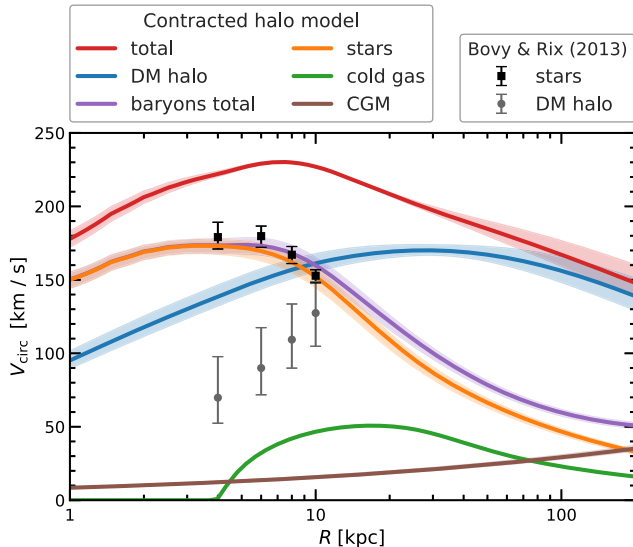
Figure 11. The rotation curve of the best fitting MW contracted NFW halo model separated into contributions from individual components. The solid lines show the maximum likelihood model and the shaded region the 68 percentile confidence regions. The symbols with error bars show the Bovy & Rix (2013) determination of the stellar disc and DM halo of the MW.

against a running average of the V_{circ} data. Such local irregularities are not allowed for in our global V_{circ} model and thus it should not be surprising that the model does not reproduce them. Secondly, at $r \sim 20$ kpc, four neighbouring data points are systematically 2-3σ below the model predictions. This could be a manifestation of systematic errors in the Eilers et al. V_{circ} data since the region $r \sim 20$ kpc is where some of their model assumptions could break down (see their Fig. 4).

The best-fitting parameter values for the contracted NFW halo model are given in the fifth column of Table 2 (see also the top right-hand corner of Fig. 12). The maximum likelihood (ML) model corresponds to the MW residing in a DM halo with mass, $M_{200}^{DM} = 0.97^{+0.24}_{-0.19} \times 10^{12}$ M$_\odot$, and concentration before baryon contraction, $c^{NFW} = 9.4^{+1.9}_{-2.6}$. The ML value for the concentration is, in fact, equal to the median concentration of $\sim 1 \times 10^{12}$ M$_\odot$ haloes (e.g. Neto et al. 2007; Hellwing et al. 2016), implying that the MW resides in an average concentration halo. Note that we did not use a prior for the concentration and thus the very good agreement between our inferred value and the theoretical predictions may be interpreted as a validation that our model gives a good description of the Galactic data.

The total mass of our galaxy is $M_{200}^{total} = 1.08^{+0.20}_{-0.14} \times 10^{12}$ M$_\odot$, in good agreement with the Callingham et al. (2019) measurement as well as other mass determinations (see fig. in Callingham et al.). As discussed previously, most of our constraints come from the V_{circ} data and thus, even though we used the Callingham et al. value in our fit, the good agreement of our M_{200}^{total} with this measurement is not guaranteed. Indeed, excluding the Callingham et al. measurement from our data sample does not introduce any systematic differences in the inferred halo mass or concentration but results in somewhat larger uncertainties.

We also find that the preferred MW stellar mass is $M_{\star \, total} = 5.04^{+0.43}_{-0.52} \times 10^{10}$ M$_\odot$, with most (three fifths) residing in the thin disc and the remainder equally split between the thick disc and the bulge

(each containing roughly one fifth of the total stellar mass). The constraints on the bulge mass are mostly given by the prior since the data we use, which corresponds to $R > 5$ kpc, is largely insensitive to the mass or geometry of the bulge (see Fig. 12). Most of the baryonic mass within the halo is in the gaseous component: 1.2×10^{10} M$_\odot$ as H I and molecular gas, and 6.4×10^{10} M$_\odot$ as the CGM. Adding up everything, we find that the MW contains roughly 72 per cent of the cosmic baryonic fraction. Caution should be taken when interpreting this result since the cold gas and especially the CGM distribution in the MW are rather uncertain. Here, we have modelled the CGM using the average predictions from hydrodynamical simulations, not taking into account halo-to-halo variation in CGM mass, which the simulations predict is rather large.

The contribution of the various MW components to the total rotation curve of the best-fitting model is shown in Fig. 11. The shaded regions around each curve show the 68 percentile confidence intervals. The inner region, $R < 10$ kpc, is dominated by baryons, in particular by the stellar component. Our inferred stellar mass is slightly smaller than the Bovy & Rix (2013) estimate, but consistent within the 68 percentile errors (see black symbols with error bars). However, we find a much more massive DM halo than Bovy & Rix. This is mostly the result of the latest *Gaia* data which favour a MW rotation curve of (229 ± 1) km s^{-1} at the Solar position, rather than the (218 ± 10) km s^{-1} value inferred by Bovy & Rix. Our results also solve a long-standing puzzle: previous measurements suggested that the MW rotation curve is dominated by the stellar component up to distances of $R \sim 12$–14 kpc (e.g. Bovy & Rix 2013; Eilers et al. 2019), in disagreement with recent hydrodynamical simulations that find that the DM should already be dominant for $R > 5$ kpc (e.g. Schaller et al. 2015; Grand et al. 2017; Lovell et al. 2018). In our model, the Galactic DM halo exceeds the stellar component contribution at $R \sim 8$ kpc, in good agreement with the theoretical predictions (see fig. 11 in Lovell et al. 2018) when accounting for the fact that the MW is a 1σ outlier in the stellar-to-halo mass relation (see discussion in Section 6.1).

To test the effect of the CGM, we have considered two variants of our MW model: (i) excluding a CGM component altogether, and (ii) assuming that the CGM mass is nearly twice as large as in the fiducial model such that the MW halo contains the universal baryonic fraction. In both cases the CGM contribution to the rotation curve is negligible for $r \lesssim 30$ kpc and hardly affects the best-fitting values of the stellar discs or the DM halo. The largest effect is on the total mass of the MW and even then the variation is small, well within the quoted uncertainty range (the total mass increases by 5 per cent in the model with the most massive CGM component compared to the model without a CGM).

To get a better understanding of the various degeneracies between the model parameters, we show in Fig. 12 the posterior distribution for each pair of parameters. In the off-diagonal panels, the red shaded regions illustrate the 68 and 95 per cent confidence regions, while, in the diagonal panels, the red lines show the marginalized probability of each model parameter. To aid the physical interpretation, we have converted the bulge and the stellar disc densities, which are the parameters used in the fitting procedure, to the total stellar mass of the bulge, thin, and thick disc, and only show these quantities in Fig. 12.

Fig. 12 shows that most parameters are weakly correlated but there are a few interesting degeneracies. Most pronounced is the degeneracy between DM halo mass and concentration. As we already discussed, most of the model constraints come from the inner regions, i.e. $r \lesssim 20$ kpc, and the same enclosed mass can be obtained by, for example, decreasing the halo concentration
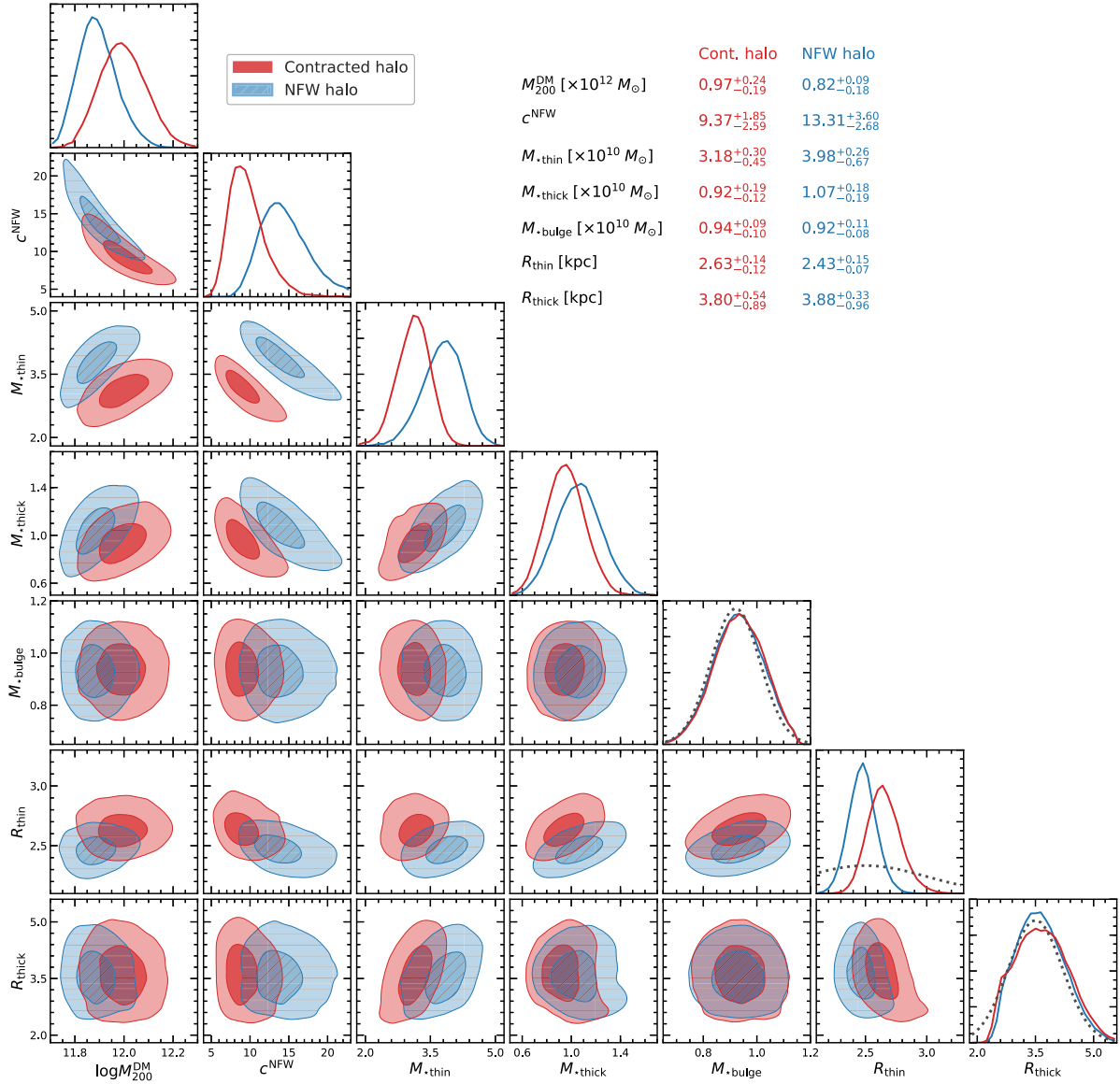
	Cont. halo	NFW halo
M_{200}^{DM} [$\times 10^{12}\,M_\odot$]	$0.97^{+0.24}_{-0.19}$	$0.82^{+0.09}_{-0.18}$
c^{NFW}	$9.37^{+1.85}_{-2.59}$	$13.31^{+3.60}_{-2.68}$
$M_{\star thin}$ [$\times 10^{10}\,M_\odot$]	$3.18^{+0.30}_{-0.45}$	$3.98^{+0.26}_{-0.67}$
$M_{\star thick}$ [$\times 10^{10}\,M_\odot$]	$0.92^{+0.19}_{-0.12}$	$1.07^{+0.18}_{-0.19}$
$M_{\star bulge}$ [$\times 10^{10}\,M_\odot$]	$0.94^{+0.09}_{-0.10}$	$0.92^{+0.11}_{-0.08}$
R_{thin} [kpc]	$2.63^{+0.14}_{-0.12}$	$2.43^{+0.15}_{-0.07}$
R_{thick} [kpc]	$3.80^{+0.54}_{-0.89}$	$3.88^{+0.33}_{-0.96}$

Figure 12. Posterior distributions pf the seven parameters of the MW mass model. The red shaded regions correspond to the contracted NFW halo model while the blue shaded regions correspond to a pure NFW halo. The darker and lighter contours enclose the 68 and 95 percentiles of the total probability respectively. The stellar masses are given in units of $10^{10}\,M_\odot$ and the disc scale lengths in kiloparsecs. For convenience, the ML values as well as the 68 percentile ranges are quoted in the top-right corner of the plot as well as in Table 2. The grey dotted lines in the last three diagonal panels show the priors for the bulge mass, and the thin and thick disc scale lengths.

in tandem with increasing the halo mass. We also find a positive correlation between halo mass and the thin and thick disc stellar masses: more massive haloes prefer a more massive stellar disc. This is because a more massive halo provides a similarly good fit only if it has a lower concentration, and thus has less mass in the inner region, which, in turn, can be compensated for by a larger disc mass. The same effect explains the negative correlation between halo concentration and disc masses, and the positive correlation between the thin and thick disc masses.

5.3.2 The pure NFW halo model

As we discussed extensively in Section 3, the accretion and settling of baryons causes a contraction of the DM halo density. Many previous studies have neglected this contraction and instead have assumed that the halo is still well fit by an NFW profile. To understand any systematic effects arising from this incorrect assumption, we proceed to fit also an NFW halo model to the same data sample.

The best fitting NFW halo model is shown by the dashed blue line in Fig. 10. We find that this model fits the data almost as well as the contracted NFW halo model (we discuss this in detail in the next subsection). In particular, in the range $r \in [4, 50]$ kpc the difference between the V_{circ} predictions of the two models is less than $1\,\mathrm{km\,s^{-1}}$. However, the best-fitting NFW model has very different parameters values than the contracted halo model. The best-fitting NFW halo has a lower mass, $M_{200}^{DM} = 0.82^{+0.09}_{-0.18} \times 10^{12}\,\mathrm{M_\odot}$, and a higher concentration, $c^{NFW} = 13.3^{+3.6}_{-2.7}$.

As we have shown in Fig. 7, the contracted NFW halo corresponding to the observed baryonic mass distribution of the MW is

not well described by an NFW profile, which raises the question: How can the NFW halo model give as good a fit to the V_{circ} data as the contracted halo model? The answer lies in the parameters describing the baryonic component of the MW, which have different values in the two models. For the pure NFW halo model, the MW total stellar mass is $5.97^{+0.40}_{-0.80} \times 10^{10}\,M_\odot$, roughly 20 per cent higher than in the contracted halo model, and, furthermore, the baryon distribution is somewhat more concentrated, with the thin disc scale length smaller in the NFW halo case. All these differences can be gauged from Fig. 12, which contrast the inferred parameters in the two models.

6 DISCUSSION

In this work we have introduced a phenomenological approach to describe the density profile of a halo that has been modified by baryons settling at its centre (see Section 3). When applied to our Galaxy, the halo contraction model predicts that the inner region contains far more DM than would have been the case in the absence of baryons. The inner regions, $r \sim 1$ kpc, see a substantial increase in enclosed DM mass while at the Sun's position the factor is ~ 2. The exact numbers depend on both the concentration and the mass of the DM halo in which our galaxy has formed: haloes with lower concentration or lower mass experience a larger contraction.

That baryons can cause a DM halo to contract has been known for a long time (Blumenthal et al. 1986; Barnes 1987), and this has been confirmed by many subsequent studies (e.g. Gnedin et al. 2004; Abadi et al. 2010; Duffy et al. 2010; Schaller et al. 2015; Dutton et al. 2016). However, Galactic studies often neglect this effect and model the DM halo as an NFW profile. While the NFW formula gives an excellent description of the DM radial density profile in DM-only simulations, it cannot capture the changes induced by the baryonic distribution. As we have shown in Section 4.2, incorrectly describing the DM halo as an NFW profile leads to biases in the inferred halo mass and concentration. These biases are largest when modelling the enclosed mass at Galactocentric distances ≤ 10 kpc; however they are non-negligible even at larger distances, or when modelling escape velocity measurements.

Using the latest Galactic rotation curve data together with a few other measurements, we have fitted a Galactic model with seven parameters, two characterizing a spherically symmetric DM halo and five the MW stellar distribution. We have found that the MW rotation curve is very well described by a contracted NFW halo with a mass of $1 \times 10^{12}\,M_\odot$ and an original (i.e. before baryonic contraction) concentration of 9, which is in remarkable agreement with the halo mass–concentration relation predicted by ΛCDM cosmological simulations (Navarro et al. 1997; Neto et al. 2007). Furthermore, our results are in very good agreement with the Li et al. (2019) recent determinations of the DM halo mass and concentration, which are based on the dynamics of MW satellites that are far enough from the Galaxy such that baryonic effects can be neglected.

The same data are also well described by a pure NFW halo but of mass, $0.8 \times 10^{12}\,M_\odot$ and concentration of 13. To fit the data, the pure NFW halo model requires the MW to have a more massive stellar disc, $\sim 5 \times 10^{10}\,M_\odot$, than inferred from the contracted halo model, $\sim 4 \times 10^{10}\,M_\odot$. This 25 per cent discrepancy is illustrated in the top panel of Fig. 13. Currently, the stellar disc mass of our galaxy is poorly constrained (e.g. see the compilation of stellar profiles in Iocco et al. 2015) and thus cannot be used to distinguish between the two models, although most measurements agree better
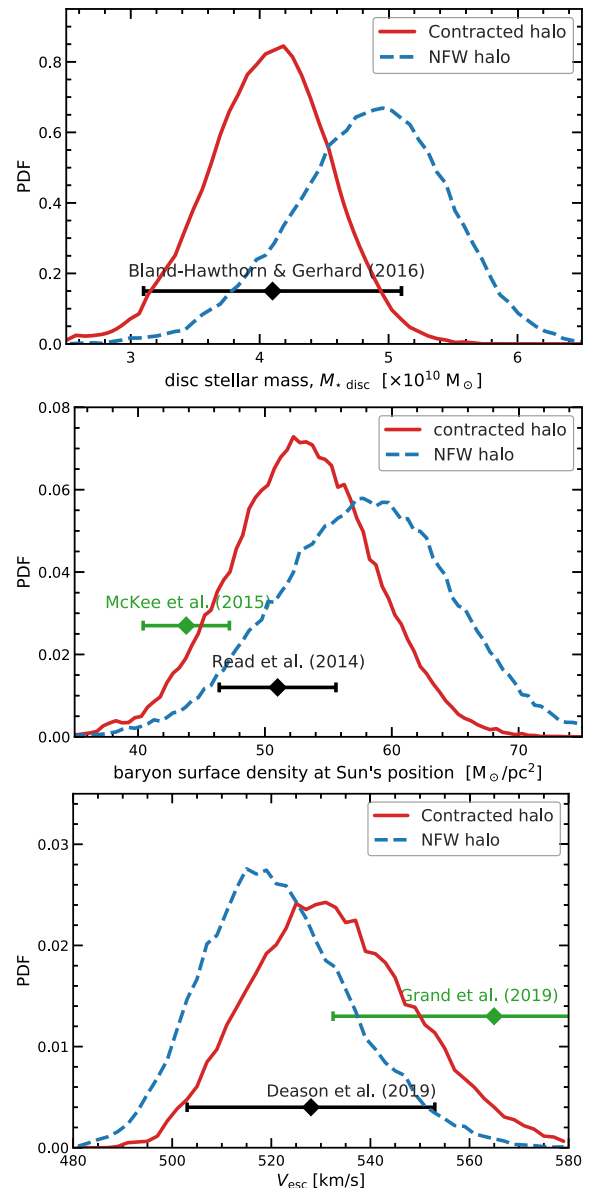

Figure 13. Examples of observables that may be used to constrain the description of the Galactic DM halo as either a contracted NFW or a pure NFW profile. The solid red and blue dashed lines show the marginalized probabilities of the observables inferred from fitting the MW rotation curve with contracted and pure NFW profiles, respectively. The three panels show: disc stellar mass (top), baryonic surface density within 1.1 kpc from the disc at the Solar position (middle), and escape velocity at the Solar position (bottom). The diamonds with horizontal error bars show recent measurements and their 68 per cent confidence limits: Bland-Hawthorn & Gerhard (2016) estimate of disc stellar mass based on a compilation of studies, Read (2014) and McKee et al. (2015) estimates of the baryonic density at the Sun's position, and the recent escape velocity measurement of Deason et al. (2019a) and the updated value of Grand et al. (2019b).

with the lower stellar mass of the contracted NFW halo model (e.g Bovy & Rix 2013; Bland-Hawthorn & Gerhard 2016). This raises an intriguing question of what kind of existing or forthcoming data can distinguish between the contracted and the pure NFW models of the Galactic DM halo? We now address this question.

6.1 Which Galactic halo model is better: a contracted NFW or a pure NFW profile?

Within the standard ΛCDM paradigm we expect, both from theoretical considerations and cosmological simulations, that the contracted halo is the physically motivated model. Nonetheless, it is desirable to check the extent to which this model is favoured by the observations.

Visually, we find that both the NFW and the contracted NFW halo models give a good fit to the MW observations analyzed in this study (see Fig. 10). The goodness of fit can be better quantified by the likelihood of the best-fitting model, and, in particular, by comparing the maximum likelihood of the two models. Both have the same number of free parameters and thus comparing them is straightforward. We find that the contracted NFW halo model is slightly preferred since it has a maximum likelihood that is a factor of 2.1 times larger than the pure NFW halo model, corresponding to a p-value of 0.48. Thus, while the contracted NFW halo model is better at describing the data, the difference is too small to rule out the pure NFW halo model.

Fig. 10 shows that while the best fitting contracted and pure NFW halo models have the same rotation curve in the region $r \in [5, 60]$ kpc, they predict different behaviours outside this region. For example, for $r < 2$ kpc, the pure NFW model predicts a rotation curve that is systematically lower by 10 km s^{-1} and thus potentially this region can be used to distinguish the two models. However, current $V_{\rm circ}$ data do not constrain the bulge mass, which in our model is mostly determined by the prior, and thus it is conceivable that, by preferring slightly different stellar bulge masses, both models could predict equal $V_{\rm circ}$ values at $r < 5$ kpc.

The contracted and pure NFW halo models also predict different $V_{\rm circ}$ values at large Galactocentric distances. At 200 kpc the contracted halo predicts a 5 km s^{-1} ($\sim$3 per cent) higher rotation velocity than the pure NFW, which potentially can be used to distinguish between the two. Current measurements at that distance are not yet accurate enough, since, for example, the Callingham et al. 2019 mass measurement has a 15 per cent uncertainty which translates into a 7.5 per cent error in $V_{\rm circ}$. The mass uncertainties could be reduced to the 10 per cent level (5 per cent in $V_{\rm circ}$) when accurate proper motions become available for most of the ultrafaint MW satellites (see fig. 11 in Callingham et al. 2019) and could be reduced even further by combining with other halo tracers such as globular clusters and halo stars.

The MW CGM is still uncertain and assuming different CGM masses could decrease the discrepancy between the models. For example, if the MW halo contained the universal baryon fraction, within 200 kpc we would expect a baryonic mass of 12.5×10^{10} M$_{\odot}$, of which slightly more than half is in the form of stars and cold dense gas at the centre of our galaxy (see Table 2). Thus, by varying the CGM mass from zero to its maximum allowed value (the universal baryon fraction; it is unlikely that a halo could contain many more baryons than the mean cosmic fraction), $V_{\rm circ}$ can vary by up to 4 per cent at $r = 200$ kpc. This variation is equal to the predicted difference between the contracted and pure NFW models at that distance and it is an important systematic that needs to be accounted for.

The best fitting contracted and pure NFW halo models imply different masses for the Galactic stellar disc, and one way to test for this is by comparing the baryonic surface density at the Solar position. In the middle panel of Fig. 13 we show the total baryon projected density within 1.1 kpc from the disc plane. The contracted NFW halo model predicts a surface density that is

Table 3. Summary of observables and measurements that can be used to choose between a contracted and a pure NFW profile as the best description of the Galactic DM halo. None of the measurements can yet be used to rule out either of the models, so here we show which of the two is preferred by each measurement, which is indicated by the ✓ symbol. The last column of gives the ratio of likelihoods between the contracted and pure NFW haloes for each measurement (a value larger than unity means that the contracted NFW halo model is preferred).

Observable	Study	Cont. halo	NFW halo	$\mathcal{L}$ ratio
Theoretical predictions[†]	–	✓	–	–
Fit to MW rotation curve	(1)	✓	–	2.1
Stellar disc mass	(2)	✓	–	1.3
Abundance matching	(3)	✓	–	2.8
	(4)	✓	–	1.9
Baryon surface density	(5)	✓	–	1.6
at Solar position	(6)	✓	–	2.3
Escape velocity	(7)	✓	–	1.1
at Solar position	(8)	✓	–	1.3

Notes. References: (1) this work, (2) Bland-Hawthorn & Gerhard (2016), (3) Moster, Naab & White (2013), (4) Behroozi, Wechsler & Conroy (2013), (5) Read (2014), (6) McKee et al. (2015), (7) Deason et al. (2019a), (8) Grand et al. (2019b).
[†]Many hydrodynamical simulations find that the DM halo profile changes in the presence of baryons (e.g. Gnedin et al. 2004; Abadi et al. 2010; Duffy et al. 2010; Schaller et al. 2015; Dutton et al. 2016).

systematically lower (by nearly 20 per cent) than the NFW halo model. The two recent determinations of Read (2014) and McKee et al. (2015) favour the contracted halo model; however, due to large uncertainties, the pure NFW model cannot be ruled out.

The escape velocity at the Solar location can also be used to differentiate between the two models, as illustrated in the bottom panel of Fig. 13. Although the two $V_{\rm esc}$ distributions overlap, the contracted NFW halo model predicts a $V_{\rm esc}$ value that is systematically higher by $\sim$10 km s^{-1}. Current $V_{\rm esc}$ measurements are not precise enough to differentiate between the two models, although the Grand et al. (2019b) value, which is an update of the Deason et al. (2019a) measurement accounting for systematics such as halo substructure and stellar halo assembly history, favours the contracted halo model.

Another way to differentiate between the two halo models is to compare them with the stellar to halo mass relation. This is a specially powerful test since the pure NFW halo model predicts a lower total mass but a higher stellar mass than the contracted NFW halo model. Using the Moster et al. (2013) abundance matching results, we find that, for the contracted NFW halo model, the MW stellar mass is 0.13 dex above the mean trend (0.9σ away). In contrast, for the pure NFW halo the stellar mass is 0.26 dex higher than the mean, a 1.7σ outlier. We obtain a similar result if instead we consider the Behroozi et al. (2013) abundance matching relation, with the MW stellar mass being 0.8 and 1.4σ above the median trend for the contracted and pure NFW halo models, respectively. The main difference between the Moster et al. and Behroozi et al. relations is that the latter has a larger scatter in the stellar mass at fixed halo mass (0.15 dex versus 0.22 dex). Thus, comparison with the stellar to halo mass relation also favours the contracted halo model but is not conclusive.

In Table 3 we provide a summary of the observables we just discussed and study the extent to which various Galactic measurements favour either the contracted or the pure NFW halo models. We calculate the joint likelihood of the measured values (assuming
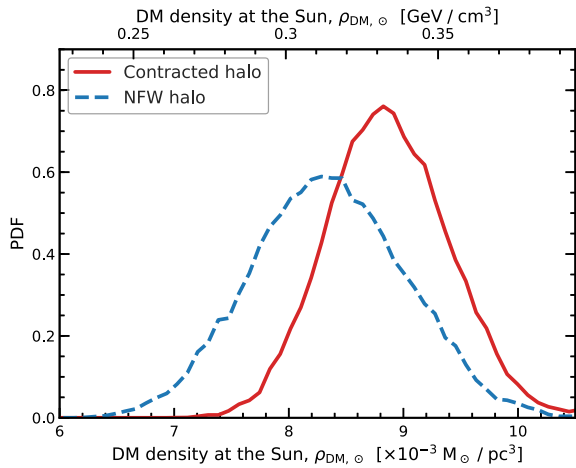
Figure 14. The DM density at the position of the Sun derived when modelling the Galactic DM halo as a contracted (solid red) or as a pure NFW halo (blue dashed). Modelling the MW as the contracted halo results in a 10 per cent higher DM density that in the pure NFW halo case.

Gaussian uncertainties) and compare with our predictions for those observables inferred using the contracted and pure NFW halo models. In all cases, we find that the contracted halo model is preferred, but due to the large uncertainties, the differences are rather modest. One way to discriminate between the two models is to calculate the joint probability of the measurements shown in Table 3. To be conservative, for each observable that has more than one entry in the table, e.g. abundance matching, we choose the entry that discriminates the least between the models. We find that the contracted NFW halo model has a 9 times higher likelihood (p-value of 0.11) than the pure NFW one.

6.2 DM density at the Solar position

One of the key products of Galactic mass models is the local density of DM, which is important for direct detection experiments. The inferred local DM density given by our model is shown in Fig. 14, where the solid and dashed lines correspond to the contracted and pure NFW halo models, respectively. The contracted halo model indicates a local DM density of $8.8^{+0.5}_{-0.5} \times 10^{-3} \, M_\odot \, pc^{-3}$, that is, $0.33^{+0.02}_{-0.02} \, GeV \, cm^{-3}$, in agreement with other literature values (e.g. see fig. 1 in the review by Read 2014). The NFW halo model predicts a DM density that is systematically lower than this by 10 per cent, which is due to the fact that the baryonic disc is more massive in that case and thus accounts for a larger fraction of the matter distribution at the Solar position. This result supports previous studies that have found that the poorly known baryonic distribution in the MW is the main systematic uncertainty in the determination of the local DM density (Buch, Chau John Leung & Fan 2019; de Salas et al. 2019; Karukes et al. 2019b). For direct detection experiments, the poorly constrained effect of baryons on the tail of the DM velocity distribution can lead to an even higher uncertainty (Bozorgnia et al. 2016, 2019; Kelso et al. 2016; Sloane et al. 2016; Callingham et al. 2020).

The comparison between the contracted and pure NFW halo models highlights the desirability of using a physically motivated global model for our Galaxy. Often, for example as we have found in Fig. 10, the data can be equally well fitted by several models that are degenerate in the properties of the baryonic and the DM components. In such cases, hydrodynamical simulations provide

an important guide by offering plausible arguments why certain models are to be preferred and thus can help break the degeneracy between the baryon and DM distributions. Our study illustrates the systematic biases in the inferred local DM distribution that can be introduced by incorrectly modelling the halo using a pure NFW profile. Biases are also likely to be present when modelling the MW halo as a gNFW profile, since this functional form is not flexible enough to capture the contracted DM halo profile (see bottom panel of Fig. 7).

6.3 The total mass of our galaxy

For the contracted halo model we find that the total mass of the MW within a radius enclosing a mean density of 200 times the critical density is $M_{200}^{total} = 1.08^{+0.20}_{-0.14} \times 10^{12} \, M_\odot$, in good agreement with many recent measurements based on the *Gaia* DR2 data (e.g. Eadie & Jurić 2019; Li et al. 2019; Posti & Helmi 2019; Wang et al. 2019; Watkins et al. 2019; Karukes et al. 2019a). While our method uses the Callingham et al. (2019) total mass measurement as one of the data points to which we fit our model, we infer roughly the same total mass if we remove the Callingham et al. data point (although with somewhat larger uncertainties). Our determination may thus be seen as a largely independent constraint on the MW total mass.

Our results also highlight that the total mass estimate is sensitive to systematic uncertainties arising from the modelling of the DM halo. Depending on which measurement is being considered, incorrectly modelling the MW halo as an uncontracted NFW profile can both overestimate or underestimate the total mass. For example, modelling the enclosed mass within a fixed Galactocentric distance as a pure NFW profile with the typical halo mass–concentration relation leads to an overestimate of the total mass (see Fig. 8; the same holds true of the escape velocity measurement but the systematic error in this case is lower – see Fig. 9). In contrast, modelling the entire rotation curve as an NFW profile leads to an underestimation of the total mass (see Table 2 and Fig. 12). This is because to account for the baryon-induced DM halo contraction, the data prefer a high concentration for the NFW profile which, given the halo mass–concentration degeneracy in the modelling, results in too low a DM halo mass. This potentially explains why mass estimates based on fitting the rotation curve (e.g. Bovy et al. 2012; Kafle et al. 2014) are systematically lower than determinations based on other methods (e.g. see the comparison in Wang et al. 2015).

6.4 Limitations and future improvements

Our model assumes a spherically symmetric DM halo but cosmological simulations predict ellipsoidal shapes (e.g. Frenk et al. 1988; Bett et al. 2007; Schneider, Frenk & Cole 2012). This simplification is unlikely to affect our results since the baryonic distribution leads to a roughly spherical DM distribution in the inner regions, i.e. for $r \lesssim 20 \, kpc$, which is the region where the best quality rotation curve data exists (Gnedin et al. 2004; Abadi et al. 2010). An approximately spherical shape for the inner Galactic halo is also supported by observational data (e.g. Posti & Helmi 2019; Wegg, Gerhard & Bieth 2019). At larger distances, the flattening of the DM halo becomes important and can affect the dynamics of halo tracers (e.g. Law & Majewski 2010; Bowden, Evans & Belokurov 2013; Shao, Cautun & Frenk 2019b). However, we have used only one measurement at such distances, the Callingham et al. (2019) total mass estimate, which is inferred under the assumption of spherical

symmetry, with deviations from this assumption being accounted for in the uncertainties and, thus, unlikely to bias our model estimates.

In fact, having a non-spherical DM halo introduces an entire new layer of complexity since both the flattening and the orientation of the MW DM halo can vary with radial distance (e.g. Bailin & Steinmetz 2005; Shao et al. 2016). In particular, based on hydro-dynamical simulations the inner halo is expected to be aligned with the Galactic disc, while the orbit of the Sagittarius stream, as well as the disc of satellite galaxies, indicate that the outer halo is perpendicular to the MW disc (Law & Majewski 2010; Vera-Ciro & Helmi 2013; Shao et al., in preparation), with the transition between the two halo orientations occurring at an as yet unconstrained distance.

As the MW data become ever more abundant and accurate, deviations from the smooth (i.e. featureless) stellar disc and halo model used here can become increasingly important. Such deviations can arise from the dynamics of the spiral arms (e.g. Hunt et al. 2018; Kawata et al. 2018), perturbations to the disc from the Sagittarius and LMC dwarfs (e.g. Gómez et al. 2017; Laporte et al. 2018), or from departures of the DM halo from equilibrium due to the recent accretion of the LMC (e.g. Erkal et al. 2018; Cautun et al. 2019; Garavito-Camargo et al. 2019), which is thought to be significantly massive, with a total mass at infall of $\sim 2.5 \times 10^{11}\,\mathrm{M}_\odot$ (Peñarrubia et al. 2016; Shao et al. 2018b). In fact, there is a dip in the MW rotation curve at $\sim 9\,\mathrm{kpc}$ from the Galactic Centre that is a several sigma outlier from the mean predictions of both the contracted and pure NFW halo models. To accommodate it, we introduced an additional model uncertainty when fitting the rotation curve data. However, this approach potentially downgrades the constraining power of the data and a better way forward would be to identify the physical cause of the deviation and model it.

7 CONCLUSIONS

We have determined the Galactic DM and baryon mass profiles using the latest *Gaia* DR2 rotation curve. We modelled the baryon distribution assuming six components: a bulge, thin and thick stellar discs, H I and molecular gas discs and a CGM. The DM halo was modelled as an NFW profile that has been contracted by the accumulation of baryons, using a prescription calibrated on the latest hydrodynamical simulations of MW-mass haloes. Throughout the paper we contrasted the results of this contracted halo model with the common approach taken in the literature of neglecting the baryon-induced contraction of the DM halo.

We first investigated the effect that baryons have on the DM distribution using three recent sets of hydrodynamical simulations of MW-mass haloes: Auriga, APOSTLE and EAGLE_recal. All of them show that the addition of baryons modifies the DM halo profile predicted by DM-only simulations and that the effect is largest at distances $r < 10\,\mathrm{kpc}$, where the enclosed DM mass can be a factor of a few to several times higher than in the absence of baryons. The change in the DM halo profile can be expressed in terms of a non-linear relation between the DM and total mass ratios (see equation 10) that is consistent across our three simulation sets (see Figs 3 and 4), and that roughly agrees with the Blumenthal et al. (1986) and Gnedin et al. (2004) adiabatic contraction approximations, although we do find systematic deviations at the 10 per cent level.

We studied the baryon-induced contraction of the Galactic DM halo to find that:

(i) Compared to the expectation from DM-only simulations, the baryons increase the enclosed DM mass by a factor of roughly 1.3, 2, and 4 times at radial distances of 20, 8, and 1 kpc respectively (see Fig. 6).

(ii) For a fixed baryonic mass, the amplitude of the contraction depends on the mass and concentration of the original (uncontracted) halo, and is larger for lower mass and lower concentration haloes (see Figs 6 and 5).

(iii) The contracted DM density profile of the MW varies as r^{-2} over a wide range of distance, $r \in [5, 30]\,\mathrm{kpc}$. The contracted profile cannot be described by NFW, gNFW, or Einasto profiles (see Fig. 7).

(iv) Incorrectly modelling the MW halo as a pure NFW profile results in systematic biases in the inferred mass and concentration of the halo (see Figs 8 and 9). These biases are present for both enclosed mass and escape velocity measurements and are largest at small r where the halo contraction is largest.

Finally, we fitted the MW mass model to the *Gaia* DR2 rotation curve as measured by Eilers et al. (2019), together with a few other measurements such as the total mass of the MW estimated by Callingham et al. (2019) and the vertical force above the disc at the Solar location given by (Kuijken & Gilmore 1991). We found that a contracted NFW DM halo model provides an excellent global fit to the MW data (see Fig. 10) and that it determines the following properties for the MW components (see Fig. 12):

(i) The Galactic DM halo has a mass of $M_{200}^{\mathrm{DM}} = 0.97^{+0.24}_{-0.19} \times 10^{12}\,\mathrm{M}_\odot$ and concentration before baryon contraction of $9.4^{+1.9}_{-2.6}$. The concentration value is identical to the median halo mass–concentration relation predicted by ΛCDM, suggesting that the MW formed in a halo of average concentration.

(ii) The MW has a total mass of $M_{200}^{\mathrm{total}} = 1.08^{+0.20}_{-0.14} \times 10^{12}\,\mathrm{M}_\odot$, in good agreement with many recent measurements based on the *Gaia* DR2 data.

(iii) The MW stellar mass is $M_{\star\,\mathrm{total}} = 5.04^{+0.43}_{-0.52} \times 10^{10}\,\mathrm{M}_\odot$, of which roughly 60 per cent is found in the thin disc, and 20 per cent each in the thick disc and the bulge. This corresponds to a bulge-to-total ratio of 0.2.

(iv) The DM density at the Solar position is $\rho_\odot^{\mathrm{DM}} = 8.8^{+0.5}_{-0.5} \times 10^{-3}\,\mathrm{M}_\odot\,\mathrm{pc}^{-3} \equiv 0.33^{+0.02}_{-0.02}\,\mathrm{GeV\,cm}^{-3}$.

While the contracted halo is the physically relevant model for the Galactic mass distribution, we have also fitted an (uncontracted) pure NFW halo model, mainly motivated by previous studies which have made this assumption. We have found that the same data are also well fit by the pure NFW halo profile but with very different properties from the contracted NFW halo model. In particular, the pure NFW halo model has a 20 per cent lower DM mass, a higher halo concentration, $c = 13.3^{+3.6}_{-2.7}$, and a more compact and 20 per cent larger stellar mass than the contracted halo model (see Fig. 12 for a detailed comparison between the two models).

The current rotation curve data used for the fit show a preference for the contracted halo model, which has two times higher maximum likelihood than the uncontracted halo. However, the difference is not large enough to rule out the pure NFW halo model. Measurements of other quantities such as the MW stellar mass, total mass, escape velocity, as well as of the stellar-to-halo mass relation, all show better matches to the contracted halo model (see discussion in Section 6.1). However, the uncertainties in current measurements are large enough that we cannot unequivocally establish if the NFW model is inconsistent with the observational data. More accurate data, particularly *Gaia* measurements of the stellar disc and H I measurements of the gaseous disc, should resolve this ambiguity.

ACKNOWLEDGEMENTS

REFERENCES

Abadi M. G., Navarro J. F., Fardal M., Babul A., Steinmetz M., 2010, MNRAS, 407, 435

Artale M. C., Pedrosa S. E., Tissera P. B., Cataldi P., Di Cintio A., 2019, A&A, 622, A197

Bailin J., Steinmetz M., 2005, ApJ, 627, 647

Barber C., Starkenburg E., Navarro J. F., McConnachie A. W., Fattahi A., 2014, MNRAS, 437, 959

Barnes J. E., 1987, in Faber S. M., ed., Nearly Normal Galaxies. From the Planck Time to the Present. Springer, Berlin, p. 154

Barnes J., White S. D. M., 1984, MNRAS, 211, 753

Behroozi P. S., Wechsler R. H., Conroy C., 2013, ApJ, 770, 57

Bett P., Eke V., Frenk C. S., Jenkins A., Helly J., Navarro J., 2007, MNRAS, 376, 215

Bissantz N., Gerhard O., 2002, MNRAS, 330, 591

Bland-Hawthorn J., Gerhard O., 2016, ARA&A, 54, 529

Blumenthal G. R., Faber S. M., Flores R., Primack J. R., 1986, ApJ, 301, 27

Bose S., Deason A. J., Frenk C. S., 2018, ApJ, 863, 123

Bovy J., 2015, ApJS, 216, 29

Bovy J., Rix H.-W., 2013, ApJ, 779, 115

Bovy J. et al., 2012, ApJ, 759, 131

Bowden A., Evans N. W., Belokurov V., 2013, MNRAS, 435, 928

Bowden A., Belokurov V., Evans N. W., 2015, MNRAS, 449, 1391

Bozorgnia N. et al., 2016, J. Cosmol. Astropart. Phys., 2016, 024

Bozorgnia N., Fattahi A., Frenk C. S., Cheek A., Cerdeno D. G., Gómez F. A., Grand R. J. J., Marinacci F., 2019, preprint (arXiv:1910.07536)

Buch J., Chau (John Leung S., Fan J., 2019, J. Cosmol. Astropart. Phys., 2019, 026

Bullock J. S., Boylan-Kolchin M., 2017, ARA&A, 55, 343

Busha M. T., Marshall P. J., Wechsler R. H., Klypin A., Primack J., 2011, ApJ, 743, 40

Callingham T. M. et al., 2019, MNRAS, 484, 5453

Callingham T. M., Cautun M., Deason A. J., Frenk C. S., Grand R. J. J., Marinacci F., Pakmor R., 2020, preprint (arXiv:2001.07742)

Cautun M., Callingham T. M., 2020, Milky Way mass profile, Zenodo, online publication

Cautun M., Frenk C. S., 2017, MNRAS, 468, L41

Cautun M., Hellwing W. A., van de Weygaert R., Frenk C. S., Jones B. J. T., Sawala T., 2014a, MNRAS, 445, 1820

Cautun M., Frenk C. S., van de Weygaert R., Hellwing W. A., Jones B. J. T., 2014b, MNRAS, 445, 2049

Cautun M., Deason A. J., Frenk C. S., McAlpine S., 2019, MNRAS, 483, 2185

Cole D. R., Binney J., 2017, MNRAS, 465, 798

Crain R. A. et al., 2015, MNRAS, 450, 1937

Davies J. J., Crain R. A., Oppenheimer B. D., Schaye J., 2020, MNRAS, 491, 4462

Davis M., Efstathiou G., Frenk C. S., White S. D. M., 1985, ApJ, 292, 371

de Salas P. F., Malhan K., Freese K., Hattori K., Valluri M., 2019, J. Cosmol. Astropart. Phys., 2019, 037

Deason A. J., Belokurov V., Evans N. W., An J., 2012, MNRAS, 424, L44

Deason A. J., Belokurov V., Koposov S. E., Gómez F. A., Grand R. J., Marinacci F., Pakmor R., 2017, MNRAS, 470, 1259

Deason A. J., Fattahi A., Belokurov V., Evans N. W., Grand R. J. J., Marinacci F., Pakmor R., 2019a, MNRAS, 485, 3514

Deason A. J., Belokurov V., Sanders J. L., 2019b, MNRAS, 490, 3426

Dehnen W., Binney J., 1998, MNRAS, 294, 429

Dekel A., Ishai G., Dutton A. A., Maccio A. V., 2017, MNRAS, 468, 1005

Di Cintio A., Brook C. B., Dutton A. A., Macciò A. V., Stinson G. S., Knebe A., 2014, MNRAS, 441, 2986

Diaz J. D., Koposov S. E., Irwin M., Belokurov V., Evans N. W., 2014, MNRAS, 443, 1688

Duffy A. R., Schaye J., Kay S. T., Dalla Vecchia C., Battye R. A., Booth C. M., 2010, MNRAS, 405, 2161

Dutton A. A. et al., 2016, MNRAS, 461, 2658

Eadie G. M., Harris W. E., 2016, ApJ, 829, 108

Eadie G., Jurić M., 2019, ApJ, 875, 159

Eadie G., Keller B., Harris W. E., 2018, ApJ, 865, 72

Eilers A.-C., Hogg D. W., Rix H.-W., Ness M. K., 2019, ApJ, 871, 120

Erkal D. et al., 2018, MNRAS, 481, 3148

Fattahi A. et al., 2016, MNRAS, 457, 844

Ferrero I. et al., 2017, MNRAS, 464, 4736

Fillingham S. P. et al., 2019, preprint (arXiv:1906.04180)

Foreman-Mackey D., Hogg D. W., Lang D., Goodman J., 2013, PASP, 125, 306

Fragione G., Loeb A., 2017, New Astron., 55, 32

Frenk C. S., White S. D. M., Davis M., Efstathiou G., 1988, ApJ, 327, 507

Fritz T. K., Battaglia G., Pawlowski M. S., Kallivayalil N., van der Marel R., Sohn S. T., Brook C., Besla G., 2018, A&A, 619, A103

Furlong M. et al., 2015, MNRAS, 450, 4486

Gaia Collaboration, 2018, A&A, 616, A1

Garavito-Camargo N., Besla G., Laporte C. F. P., Johnston K. V., Gómez F. A., Watkins L. L., 2019, ApJ, 884, 51

Gibbons S. L. J., Belokurov V., Evans N. W., 2014, MNRAS, 445, 3788

Gnedin O. Y., Kravtsov A. V., Klypin A. A., Nagai D., 2004, ApJ, 616, 16

Gnedin O. Y., Brown W. R., Geller M. J., Kenyon S. J., 2010, ApJ, 720, L108

Gómez F. A., White S. D. M., Grand R. J. J., Marinacci F., Springel V., Pakmor R., 2017, MNRAS, 465, 3446

Grand R. J. J. et al., 2017, MNRAS, 467, 179

Grand R. J. J. et al., 2019a, MNRAS, 490, 4786

Grand R. J. J., Deason A. J., White S. D. M., Simpson C. M., Gómez F. A., Marinacci F., Pakmor R., 2019b, MNRAS, 487, L72

Gravity Collaboration, 2018, A&A, 615, L15

Hani M. H., Ellison S. L., Sparre M., Grand R. J. J., Pakmor R., Gomez F. A., Springel V., 2019, MNRAS, 488, 135

Hellwing W. A., Frenk C. S., Cautun M., Bose S., Helly J., Jenkins A., Sawala T., Cytowski M., 2016, MNRAS, 457, 3492

Heyer M., Dame T. M., 2015, ARA&A, 53, 583

Hogg D. W., Eilers A.-C., Rix H.-W., 2019, AJ, 158, 147

Hunt J. A. S., Hong J., Bovy J., Kawata D., Grand R. J. J., 2018, MNRAS, 481, 3794

Iocco F., Pato M., Bertone G., 2015, Nat. Phys., 11, 245

Jurić M. et al., 2008, ApJ, 673, 864

Kafle P. R., Sharma S., Lewis G. F., Bland-Hawthorn J., 2012, ApJ, 761, 98

Kafle P. R., Sharma S., Lewis G. F., Bland-Hawthorn J., 2014, ApJ, 794, 59

Kahlhoefer F., Kaplinghat M., Slatyer T. R., Wu C.-L., 2019, J. Cosmol. Astropart. Phys., 2019, 010

Kalberla P. M. W., Dedes L., 2008, A&A, 487, 951

Karukes E. V., Benito M., Iocco F., Trotta R., Geringer-Sameth A., 2019a, preprint (arXiv:1912.04296)

Karukes E. V., Benito M., Iocco F., Trotta R., Geringer-Sameth A., 2019b, J. Cosmol. Astropart. Phys., 2019, 046

Kawata D., Baba J., Ciucǎ I., Cropper M., Grand R. J. J., Hunt J. A. S., Seabroke G., 2018, MNRAS, 479, L108

Kelso C., Savage C., Valluri M., Freese K., Stinson G. S., Bailin J., 2016, J. Cosmol. Astropart. Phys., 2016, 071

Kennedy R., Frenk C., Cole S., Benson A., 2014, MNRAS, 442, 2487

Klypin A., Zhao H., Somerville R. S., 2002, ApJ, 573, 597

Klypin A., Yepes G., Gottlöber S., Prada F., Heß S., 2016, MNRAS, 457, 4340

Komatsu E. et al., 2011, ApJS, 192, 18

Kuijken K., Gilmore G., 1991, ApJ, 367, L9

Laporte C. F. P., Johnston K. V., Gómez F. A., Garavito-Camargo N., Besla G., 2018, MNRAS, 481, 286

Law D. R., Majewski S. R., 2010, ApJ, 714, 229

Li Y.-S., White S. D. M., 2008, MNRAS, 384, 1459

Li Z.-Z., Jing Y. P., Qian Y.-Z., Yuan Z., Zhao D.-H., 2017, ApJ, 850, 116

Li Z.-Z., Qian Y.-Z., Han J., Li T. S., Wang W., Jing Y. P., 2019, preprint (arXiv:1912.02086)

Lin H.-N., Li X., 2019, MNRAS, 487, 5679

Lovell M. R., Frenk C. S., Eke V. R., Jenkins A., Gao L., Theuns T., 2014, MNRAS, 439, 300

Lovell M. R. et al., 2018, MNRAS, 481, 1950

Ludlow A. D., Navarro J. F., Angulo R. E., Boylan-Kolchin M., Springel V., Frenk C., White S. D. M., 2014, MNRAS, 441, 378

Ludlow A. D., Schaye J., Bower R., 2019a, MNRAS, 488, 3663

Ludlow A. D., Schaye J., Schaller M., Richings J., 2019b, MNRAS, 488, L123

Marinacci F., Grand R. J. J., Pakmor R., Springel V., Gómez F. A., Frenk C. S., White S. D. M., 2017, MNRAS, 466, 3859

Mateu C., Vivas A. K., 2018, MNRAS, 479, 211

McKee C. F., Parravano A., Hollenbach D. J., 2015, ApJ, 814, 13

McMillan P. J., 2011, MNRAS, 414, 2446

McMillan P. J., 2017, MNRAS, 465, 76

Monachesi A. et al., 2019a, MNRAS, 485, 2589

Monachesi A. et al., 2019b, MNRAS, 485, 2589

Monari G. et al., 2018, A&A, 616, L9

Moster B. P., Naab T., White S. D. M., 2013, MNRAS, 428, 3121

Navarro J. F., Frenk C. S., White S. D. M., 1996, ApJ, 462, 563

Navarro J. F., Frenk C. S., White S. D. M., 1997, ApJ, 490, 493

Neto A. F. et al., 2007, MNRAS, 381, 1450

Nightingale J. W., Dye S., Massey R. J., 2018, MNRAS, 478, 4738

Patel E., Besla G., Mandel K., 2017, MNRAS, 468, 3428

Pedrosa S., Tissera P. B., Scannapieco C., 2010, MNRAS, 402, 776

Peñarrubia J., Benson A. J., Walker M. G., Gilmore G., McConnachie A. W., Mayer L., 2010, MNRAS, 406, 1290

Peñarrubia J., Gómez F. A., Besla G., Erkal D., Ma Y.-Z., 2016, MNRAS, 456, L54

Pieres A. et al., 2019, preprint (arXiv:1904.04350)

Piffl T. et al., 2014, A&A, 562, A91

Piffl T., Penoyre Z., Binney J., 2015, MNRAS, 451, 639

Planck Collaboration XVI, 2014, A&A, 571, A1

Portail M., Gerhard O., Wegg C., Ness M., 2017, MNRAS, 465, 1621

Posti L., Helmi A., 2019, A&A, 621, A56

Pouliasis E., Di Matteo P., Haywood M., 2017, A&A, 598, A66

Power C., Navarro J. F., Jenkins A., Frenk C. S., White S. D. M., Springel V., Stadel J., Quinn T., 2003, MNRAS, 338, 14

Purcell C. W., Zentner A. R., 2012, J. Cosmol. Astropart. Phys., 2012, 007

Read J. I., 2014, J. Phys. G: Nucl. Phys., 41, 063101

Rossi E. M., Marchetti T., Cacciato M., Kuiack M., Sari R., 2017, MNRAS, 467, 1844

Sawala T. et al., 2016a, MNRAS, 456, 85

Sawala T. et al., 2016b, MNRAS, 457, 1931

Schaller M. et al., 2015, MNRAS, 451, 1247

Schaye J. et al., 2015, MNRAS, 446, 521

Schneider M. D., Frenk C. S., Cole S., 2012, J. Cosmol. Astropart. Phys., 2012, 030

Sellwood J. A., McGaugh S. S., 2005, ApJ, 634, 70

Shao S., Cautun M., Frenk C. S., Gao L., Crain R. A., Schaller M., Schaye J., Theuns T., 2016, MNRAS, 460, 3772

Shao S., Cautun M., Frenk C. S., Grand R. J. J., Gómez F. A., Marinacci F., Simpson C. M., 2018a, MNRAS, 476, 1796

Shao S., Cautun M., Deason A. J., Frenk C. S., Theuns T., 2018b, MNRAS, 479, 284

Shao S., Cautun M., Frenk C. S., 2019b, MNRAS, 488, 1166

Simpson C. M., Grand R. J. J., Gómez F. A., Marinacci F., Pakmor R., Springel V., Campbell D. J. R., Frenk C. S., 2018, MNRAS, 478, 548

Sloane J. D., Buckley M. R., Brooks A. M., Governato F., 2016, ApJ, 831, 93

Smith M. C. et al., 2007, MNRAS, 379, 755

Springel V., 2005, MNRAS, 364, 1105

Springel V., 2010, MNRAS, 401, 791

Springel V., Yoshida N., White S. D. M., 2001, New Astron., 6, 79

Trayford J. W. et al., 2015, MNRAS, 452, 2879

Tumlinson J., Peeples M. S., Werk J. K., 2017, ARA&A, 55, 389

Vera-Ciro C., Helmi A., 2013, ApJ, 773, L4

Vogelsberger M., Zavala J., Loeb A., 2012, MNRAS, 423, 3740

Wang J., Frenk C. S., Navarro J. F., Gao L., Sawala T., 2012, MNRAS, 424, 2715

Wang W., Han J., Cooper A. P., Cole S., Frenk C., Lowing B., 2015, MNRAS, 453, 377

Wang W., Han J., Cole S., Frenk C., Sawala T., 2017, MNRAS, 470, 2351

Wang W., Han J., Cole S., More S., Frenk C., Schaller M., 2018, MNRAS, 476, 5669

Wang W., Han J., Cautun M., Li Z., Ishigaki M. N., 2019, preprint (arXiv:1912.02599)

Watkins L. L., Evans N. W., An J. H., 2010, MNRAS, 406, 264

Watkins L. L., van der Marel R. P., Sohn S. T., Evans N. W., 2019, ApJ, 873, 118

Weber M., de Boer W., 2010, A&A, 509, A25

Wegg C., Gerhard O., Bieth M., 2019, MNRAS, 485, 3296

White S. D. M., Frenk C. S., 1991, ApJ, 379, 52

Xue X. X. et al., 2008, ApJ, 684, 1143

Zavala J., Frenk C. S., 2019, Galaxies, 7, 81

APPENDIX A: THE INFERRED MW MASS PROFILE

The best parameter values of our MW mass model and their implementation in the `galpy` code (Bovy 2015) are publicly available at https://github.com/MariusCautun/Milky_Way_mass_profile. For ease of use, we also present the inferred profiles in Table A1.

Table A1. The spherically averaged *enclosed* mass profile of our galaxy inferred in this work. The table gives the maximum likelihood value and the 68 percentile confidence regions for the enclosed stellar, $M_\star^{\rm MW}$, baryonic, $M_{\rm bar}^{\rm MW}$, DM, $M_{\rm DM}^{\rm MW}$, and total, $M_{\rm total}^{\rm MW}$, mass as a function of radial distance from the Galactic Centre, r. The baryonic mass includes stars, HI, molecular gas and CGM (see Section 2 for details). The results are for our physically motivated contracted halo model. We only fit data in the range, $r \in [4, 220]$ kpc, and the values outside this interval are model extrapolations.

r [kpc]	$M_\star^{\rm MW}(<r)$ [10^{10} M$_\odot$]	$M_{\rm bar}^{\rm MW}(<r)$ [10^{10} M$_\odot$]	$M_{\rm DM}^{\rm MW}(<r)$ [10^{10} M$_\odot$]	$M_{\rm total}^{\rm MW}(<r)$ [10^{10} M$_\odot$]
1	$0.59^{+0.03}_{-0.04}$	$0.59^{+0.03}_{-0.04}$	$0.21^{+0.03}_{-0.02}$	$0.80^{+0.04}_{-0.04}$
2	$1.39^{+0.07}_{-0.09}$	$1.40^{+0.07}_{-0.09}$	$0.65^{+0.09}_{-0.07}$	$2.04^{+0.07}_{-0.07}$
3	$2.04^{+0.10}_{-0.13}$	$2.07^{+0.11}_{-0.13}$	$1.18^{+0.15}_{-0.12}$	$3.26^{+0.07}_{-0.07}$
5	$3.06^{+0.19}_{-0.22}$	$3.19^{+0.19}_{-0.22}$	$2.45^{+0.27}_{-0.22}$	$5.64^{+0.07}_{-0.05}$
8	$4.07^{+0.29}_{-0.34}$	$4.41^{+0.30}_{-0.34}$	$4.59^{+0.43}_{-0.36}$	$8.99^{+0.09}_{-0.07}$
10	$4.45^{+0.34}_{-0.40}$	$4.93^{+0.34}_{-0.40}$	$6.06^{+0.51}_{-0.43}$	$10.98^{+0.12}_{-0.10}$
15	$4.88^{+0.40}_{-0.48}$	$5.67^{+0.41}_{-0.49}$	$9.72^{+0.65}_{-0.56}$	$15.38^{+0.18}_{-0.16}$
20	$4.99^{+0.42}_{-0.51}$	$6.03^{+0.44}_{-0.52}$	$13.31^{+0.73}_{-0.63}$	$19.34^{+0.29}_{-0.25}$
25	$5.03^{+0.43}_{-0.52}$	$6.26^{+0.46}_{-0.53}$	$16.80^{+0.80}_{-0.67}$	$23.06^{+0.47}_{-0.41}$
30	$5.03^{+0.44}_{-0.52}$	$6.42^{+0.46}_{-0.53}$	$20.18^{+0.94}_{-0.74}$	$26.60^{+0.74}_{-0.63}$
40	$5.04^{+0.44}_{-0.52}$	$6.67^{+0.48}_{-0.55}$	$26.6^{+1.4}_{-1.1}$	$33.3^{+1.5}_{-1.2}$
50	$5.04^{+0.44}_{-0.52}$	$6.89^{+0.50}_{-0.56}$	$32.5^{+2.2}_{-1.7}$	$39.4^{+2.4}_{-2.0}$
60	$5.04^{+0.44}_{-0.52}$	$7.12^{+0.52}_{-0.57}$	$38.0^{+3.2}_{-2.5}$	$45.1^{+3.4}_{-2.8}$
70	$5.04^{+0.44}_{-0.52}$	$7.36^{+0.55}_{-0.58}$	$43.1^{+4.2}_{-3.3}$	$50.5^{+4.5}_{-3.6}$
80	$5.04^{+0.44}_{-0.52}$	$7.63^{+0.57}_{-0.58}$	$47.9^{+5.2}_{-4.0}$	$55.6^{+5.6}_{-4.4}$
90	$5.04^{+0.44}_{-0.52}$	$7.90^{+0.60}_{-0.62}$	$52.4^{+6.3}_{-4.8}$	$60.3^{+6.8}_{-5.2}$
100	$5.04^{+0.44}_{-0.52}$	$8.20^{+0.63}_{-0.64}$	$56.7^{+7.4}_{-5.5}$	$64.9^{+7.9}_{-6.0}$
125	$5.04^{+0.44}_{-0.52}$	$9.0^{+0.7}_{-0.7}$	66^{+10}_{-7}	75^{+11}_{-8}
150	$5.04^{+0.44}_{-0.52}$	$9.9^{+0.8}_{-0.8}$	75^{+13}_{-9}	85^{+13}_{-10}
175	$5.04^{+0.44}_{-0.52}$	$10.9^{+0.9}_{-0.8}$	83^{+15}_{-11}	94^{+16}_{-11}
200	$5.04^{+0.44}_{-0.52}$	$12.0^{+1.1}_{-0.9}$	90^{+17}_{-12}	102^{+18}_{-13}
225	$5.04^{+0.44}_{-0.52}$	$13.1^{+1.2}_{-1.0}$	96^{+19}_{-14}	109^{+20}_{-14}
250	$5.04^{+0.44}_{-0.52}$	$14.3^{+1.3}_{-1.1}$	102^{+21}_{-15}	117^{+22}_{-16}
275	$5.04^{+0.44}_{-0.52}$	$15.6^{+1.5}_{-1.2}$	108^{+23}_{-16}	124^{+24}_{-17}
300	$5.04^{+0.44}_{-0.52}$	$17.0^{+1.7}_{-1.3}$	114^{+25}_{-17}	131^{+26}_{-19}

APPENDIX B: UNCERTAINTIES ASSOCIATED WITH FITTING A MW MODEL

As we have argued in the main text, our goal is to find a global best-fitting model of our galaxy. Models are often simplified versions of the complex processes affecting observations so there could be residual features in the data that manifest themselves as a reduced χ^2 greater than 1. For example, structures in our galaxy, such as spiral arms, can affect the rotation curve measurements but they are not captured by the model studied here. As long as these fluctuations do no induce systematic changes in the rotation curve, we can account for them by adding an additional model uncertainty (e.g. see Nightingale, Dye & Massey 2018, in the context of gravitational lensing).

We use the data themselves to find the additional model uncertainty. To do so, we add a nuisance parameter to our model whose role is to quantify the size of the additional errors needed so that our best fit model returns a reduced χ^2 of order unity. We have explored two different parametrizations for this nuisance parameter. First, we assume that this additional uncertainty is the same for all data points. Then, the error of each data point is the sum in quadrature of the Eilers et al. (2019) observational error, $\sigma_{\rm obs}$ and this constant value, σ_0, i.e. $\sigma = \sqrt{\sigma_{\rm obs}^2 + \sigma_0^2}$. In a second approach, we assume that the additional uncertainty can vary between the data points. For example, this could be due to the various assumptions made when determining the rotation curve, with Eilers et al. showing that these errors grow from 2 per cent for $R < 15$ kpc to $\sim$10 per cent for $R > 20$ kpc. Assuming that the Eilers et al. systematic is the dominant source of deviation between our model and the data motives us to increase the rotation curve errors by adding a contribution proportional to the Eilers et al. systematic errors, $\sigma_{\rm sys}$. In this case, the total error for each data point is given by $\sigma = \sqrt{\sigma_{\rm obs}^2 + (\mu \sigma_{\rm sys})^2}$, where μ denotes the nuisance parameter that we vary.

We estimate the optimal value of the nuisance parameter by finding the value that maximizes the likelihood. This works as follows. For a given model, the probability for an observation to have value y is given by

$$\frac{1}{\sqrt{2\pi}\sigma} \exp \frac{(y - y_{\rm model})^2}{2\sigma}, \tag{B1}$$

where $y_{\rm model}$ denotes the model prediction and σ the measurement plus the model uncertainty. Increasing the model uncertainty has two effects. A small value mostly affects the exponential term and can lead to a higher overall probability. However, too large a value for the model uncertainty hardly affects the exponential term, which will be close to unity, and will decrease the overall probability due to σ appearing in the factor in front of the exponential. Thus, there is an optimal value of the model uncertainty that will maximize the probability.

To find the optimal value of the model uncertainty, which is parametrized in terms of σ_0 or μ, we run the MCMC algorithm using eight parameters: σ_0 (or μ) plus the seven parameters described in Section 5. The likelihood is maximized for $\sigma_0 = 1.2$ km s^{-1} for the first parametrization of the error and for $\mu = 0.21$ for the second parametrization (we actually obtain a range of values for σ_0 and μ, but choose only the MLE). Then, we rerun the MCMC method but now keeping σ_0 (or μ) fixed to their MLE values.

Fig. B1 shows the PDF for the seven MW parameters varied in our model. Each panel contains three curves corresponding to the case where we consider the original Eilers et al. (2019) errors and to the two cases where we add a model uncertainty to obtain a reduced χ^2 close to unity. While we find some differences in the parameter distributions, these are rather small, especially for the two cases with model uncertainties. This indicates that our results are not sensitive to the approach employed to obtain a model that gives a good global fit to the data. In our analysis, we choose the second approach to increasing the error, i.e. $\sigma = \sqrt{\sigma_{\rm obs}^2 + (\mu \sigma_{\rm sys})^2}$, since it predicts larger uncertainties at large distances, i.e. $R > 20$ kpc. In that region, the Eilers et al. (2019) rotation curve shows a dip that is a few sigma away from the best fitting global model.
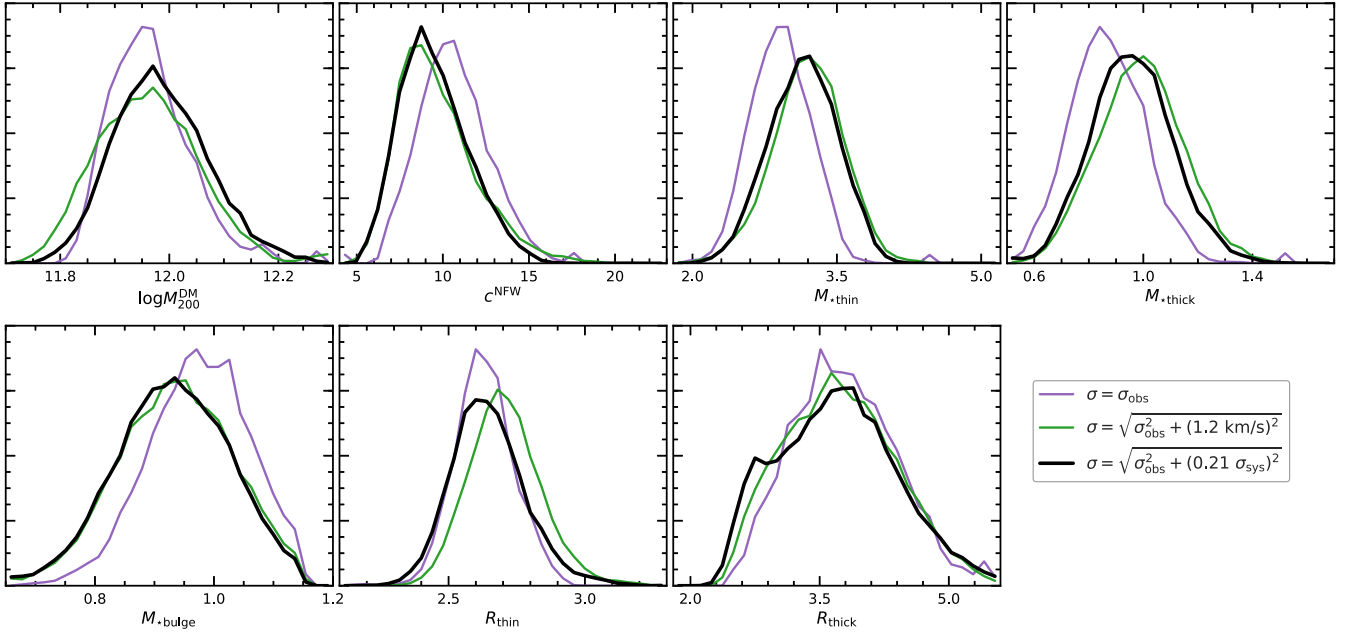
Figure B1. The marginalized PDF for the seven parameters used to describe the MW mass profile. Here we show the effect of adding model uncertainties to obtain a global fit with a reduced χ^2, close to unity. All approaches that include a model uncertainty (green and black curves) give roughly the same PDFs. The purple curve corresponds to finding the best fitting model in the absence of model uncertainties, i.e. using only the Eilers et al. (2019) observational errors. In this case, the best fit model has a reduced $\chi^2 \simeq 2$. To obtain best fits with reduced $\chi^2 \simeq 1$, we add model uncertainties in two ways: (i) by adding in quadrature a constant error of $1.2\,\mathrm{km\,s^{-1}}$ to each data point (green curve), and (ii) by adding in quadrature an uncertainty of $0.21\sigma_{\mathrm{sys}}$ (black curve; this is the default approach used in our analysis), where σ_{sys} is the systematic error associated with the Eilers et al. rotation curve.

This paper has been typeset from a TEX/LATEX file prepared by the author.